MÖSSBAUER STUDY OF THE HYPERFINE MAGNETIC FIELD AND ELECTRIC FIELD GRADIENT AT Fe SITES IN SYNTHETIC DIAMOND.

Nadaraj Govender

MÖSSBAUER STUDY OF THE HYPERFINE MAGNETIC FIELD AND ELECTRIC FIELD GRADIENT AT Fe SITES IN SYNTHETIC DIAMOND.

Nadaraj Govender

Submitted to the Faculty of Science, University of Durban-Westville in partial fulfilment of the requirements for the Degree of Master of Science in Physics.

Supervisor : Professor K Bharuth-Ram

Date submitted : December 1992

ABSTRACT

Mössbauer Spectroscopy has been used to investigate the site of Fe inclusions in a suite of synthetic diamonds (de Beers MDAS). Information on the hyperfine magnetic fields and electric field gradients at Fe sites in the diamond grains were obtained from Mössbauer Spectroscopy of diamond grains ranging in size from 25 to 250 μm. The Fe inclusions in these samples resulted from the synthesis of the diamond grains in which Fe was used as a catalytic solvent. The Mössbauer measurements were carried at room temperature with a constant acceleration spectrometer operating in transmission geometry.

The samples with the largest grain size of 180-250 μm gave a well defined six component magnetically split spectrum, similar to the Zeeman split sextet obtained for natural iron. As the grain sizes decreased the intensity of the magnetically split components became greatly reduced and a strong paramagnetic component appeared. At grain sizes 105-45 μm the spectra are dominated by a central single line with some evidence of an asymmetric doublet.

For the finest grain size 38-25 μm, the reappearance of the six magnetic hyperfine splitting components together with the strong central single paramagnetic component was observed.

The change in the Mössbauer patterns observed with decreasing grain size suggest that a rapid phase transition of the Fe inclusions from ferromagnetic to superparamagnetic takes place.

The analysis of Mössbauer spectra yielded a value of the hyperfine magnetic field of B_{hf} = -32.4(4) T and an electric field gradient in the range of V_{zz} = 1.4(4) - 1.8(7) x 10^{18} V.cm^{-2} at the site of the probe ^{57}Fe nucleus. These values compare favourably with other measurements.

ACKNOWLEDGEMENTS

I would like to thank the following :

My supervisor Professor K Bharuth-Ram for the guidance, motivation and helpful suggestions offered during the period of this study.

Mr H. Haricharan and Mr V.V Naicker for their computational assistance.

My wife, Sarojini Govender for her patience and support during the course of my research.

The University of Durban-Westville for the financial support.

Professor J.P.F. Sellschop and Messrs de Beers Industrial Diamonds (Pty) Ltd. for the diamond samples used in this research and their support.

The typist, Mrs D. Pillay and the secretary of the Physics Department, Miss Debba for her kind assistance.

TABLE OF CONTENTS

LIST OF FIGURES

LIST OF TABLES

1. INTRODUCTION

1.1 THE PHYSICAL PROPERTIES OF DIAMOND

Diamond is composed of the single element carbon. It has exceptional physical properties such as extreme hardness (maximum rating on the Moh's scale of hardness), chemical inertness, compressive strength, high thermal conductivity, poor electrical conductivity and a small atomic volume. The main properties of diamond are given in Table 1.1. below.

Table 1.1 The properties of diamond.

Debye temperature	Θ_D = 2000 K
heat conductivity (300 K)	2000 $W.m^{-1}$
heat capacity (300 K)	501.6 $J.kg^{-1}$
melting point	> 3550 °C
boiling point	4827 °C
density	3520 $kg.m^{-3}$
refractive index	2.42
dielectric permeability	5.86

These properties indicate that the atoms in the crystal are bonded very strongly to form a rigid structure. The small interatomic distance and strong covalent bonding between carbon atoms render the diamond structure inhospitable to individual substitutional or interstitial impurity atoms.

Due to these properties, diamond is a most versatile abrasive material employed in industrial applications such as in turning and cutting tools and diamond dies. Natural diamonds, being rare and expensive have been supplemented by industrial diamonds (synthetic) which have similar properties and are produced at low cost.

Diamonds are classified into two types viz., Type I and Type II, following the classification of Custers (1952) for natural diamonds [Fi79]. The two types are distinguished by their absorption features in the ultra-violet and infra-red regions. Diamonds that lack infra-red absorption are classified as Type II. Types Ib diamonds produce an electron spin resonance (ESR) signal, Type Ia do not. Type IIa are electrical insulators while IIb stones are semi-conductors. In contrast to natural Type I diamonds, synthetic diamonds are invariably of Type Ib. By deliberately introducing dopants e.g., boron, into the synthesis starting materials, it is possible to group diamonds which exhibit semiconducting properties. In boron-doped synthetic type IIb diamonds, electrical conductivity has been measured [Ma78].

The recent fabrication of diamond by chemical vapour deposition (CVD) has the potential of expanding the applications of diamonds e.g. fabricating light-emitting, high temperature, high power semiconducting devices, etc. [Ka90].

The increasing industrial applications of diamond has given impetus to microscopic studies of their physical properties. Investigations on the causes of the characteristic behaviour of the different types of diamonds lead naturally to attempts to produce synthetic diamonds with selected properties.

Synthetic diamonds have been used widely in the abrasive industry but its non-abrasive use is now being extensively researched. It is of significant interest to improve our understanding of their electronic properties as they are modified by impurities and defects. Diamonds can be insulators or high band-gap semiconductors. Contemporary data on the band structure, transport phenomena and other electronic and optical processes in insulating and semiconducting diamonds stimulates the research directed towards controlling the properties of this material. The final lattice site of the impurity or inclusion in diamond and its possible association with defects will determine the electronic properties of the semi-conductor.

This thesis describes a Mössbauer study of Fe inclusions in MDAS (Micron Diamond Abrasive) diamond grains ranging in size from 25 to 250 μm. The samples were supplied by de Beers Industrial Diamonds (Pty) Limited, and were produced by the solvent-catalyst technique in which Fe was used as a catalyst. The Fe inclusions were thus entrapped in the diamond lattice during synthesis.

1.2 THE GROWTH OF SYNTHETIC DIAMONDS.

In principle, diamond growth is like any other crystal growth process in that it is completely defined by the basic thermodynamic variables: temperature, pressure and composition.

In the solvent-catalyst method, graphite is dissolved in a metal solvent in order to reduced the energetic threshold for the conversion of graphite to diamond to a value close to the thermodynamic equilibrium. As the reaction takes place at the liquid-solid interface this process has its limit defined by the lowest possible melting temperature for the metal-carbon mixture.

The function of the solvent is to dissolve the carbon source material by breaking up the bonds between groups of carbon atoms, and to transport this material to the growing diamond.

Two different kinds of solvents can be distinguished: the first form a pure eutectic system with both allotropes of carbon while the second form carbides at least at diamond synthesis conditions.

Nickel is an example of the former type of solvent while iron, is representative of the carbide formers.

From the calculated iron-carbon phase diagram the

approximate minimum pressure for a stable diamond phase is estimated to be 5.7 GPa [We79]. The Fe-C phase diagrams indicate that the compostion at the three phase cementite-diamond-liquid equilibrium point is less then 25% carbon.

As the pressure increases this three-phase point moves to higher carbon compositions which lowers the minimum temperature for diamond synthesis [We79].

Bradley [We79], showed that the diamond-graphite interfacial energy plays a decisive role in the formation of a critical nucleus which leads to the formation of diamond. Cannon and Conlin [We79], investigated the problem of whether diamond nucleates heterogeneously or homogeneously in the solvent-catalyst process and came to the conclusion that certain components e.g., boron, can encourage or poison nucleation. The above studies indicated that this might be due to ionized carbon atoms that are involved in the formation of nuclei. Surface properties and contact angles of various transition metals, and carbon solutions in transition metals are important to nucleation behaviour as the interfacial energy has a prime influence on the nucleation energy for a critical nucleus.

Since a thin skin of solvent material was always found around recovered diamonds [We79], it was therefore accepted that the mechanism controlling the maximum growth rate is given by the diffusion of carbon through the

metal matrix, which is normally not saturated with carbon.

Giardini and Tydings [We79], postulated that for a number of solvent systems (Mn, Fe, Co, etc.,) the formation of diamond occurs via a transition state of a carbon-rich carbide which then decomposes into diamond and a thermodynamically more stable carbide of lesser carbon content.

This transition state theory for diamond growth would explain the presence of carbide in the thin metallic layer around the grown crystal. However, there is also evidence that simple diffusion takes place across the metallic layer. Strong and Hanneman [We79], demonstrated this by showing that the growth rate is proportional to the growth time and inversely proportional to the thickness of the metal skin. This is in agreement with the other findings that carbon is deposited on the growing diamond surface as isolated atoms [Ca62].

Further proposals are that diamond forms via an intermediate state where the metal solvent has been dissolved in graphite as an intercalation compound.

The graphite starting material is thus broken up into monolayers which subsequently rearrange to form diamond with a metal content. Finally, the metal diffuses out of the supersaturated diamond crystal leaving only a small

fraction in solution while most of the metal forms the skin around the crystal and some metal gets trapped as inclusions.

Vereshchagin et al. [We79], tried to reconcile this model with the solvent theory adopted for diamond synthesis. They suggested that the carbon starting material goes into solution until the liquid metal is saturated. In addition, clusters of carbon are found in the liquid which resemble the crystal structure of the starting carbon.

1.3 THE TECHNOLOGY OF DIAMOND GROWTH.

The experimental problem of growing diamonds is essentially one of designing an apparatus capable of producing and sustaining pressures greater than 6.0 GPa and temperatures greater than 1600 K.

The problem which was a kinetic one, i.e., of overcoming the very large kinetic barrier that separates sp^2 hybridized graphite from sp^3 hybridized diamond was solved by a group of scientists working at the ASEA laboratory in Stockholm, Sweden in 1953. Independently, in 1955, Bundy, Hall, Strong and Wentorf at the General Electric laboratories [We79], were also successful in producing synthetic diamonds. Both groups used a carbon solvent/catalyst, which acted as a transport agent for carbon, to overcome the large kinetic barrier.

The exact method one uses to grow diamonds depends upon the type of diamonds required. There are several techniques in which diamonds are synthesised. These are :

(1) the solvent-catalyst method,

(2) the reconstitution technique,

(3) shockwave synthesis,

(4) epitaxial growth,

(5) vapour-liquid-solid (VLS) growth and

(6) chemical vapour deposition (CVD).

(1) The solvent-catalyst method.

In this case, diamond synthesis is reduced to getting the carbon into the correct thermodynamic region, in the presence of a suitable solvent-catalyst. The carbonaceous material, usually graphite, is mixed and compacted with a suitable solvent catalyst (e.g., Ni, Co, Fe) into the reaction chamber of a diamond synthesis apparatus.
This reaction volume is then compressed to over 6 GPa and heated to above the eutectic melting point of the solvent (about 1500 K) [We79]. If the above conditions are achieved then diamonds will precipitate from the solution
The belt type apparatus (Figure 1.1 a) or a tetrahedral apparatus (Figure 1.1 b), are typical of those used in diamond synthesis experiments [Fi79].

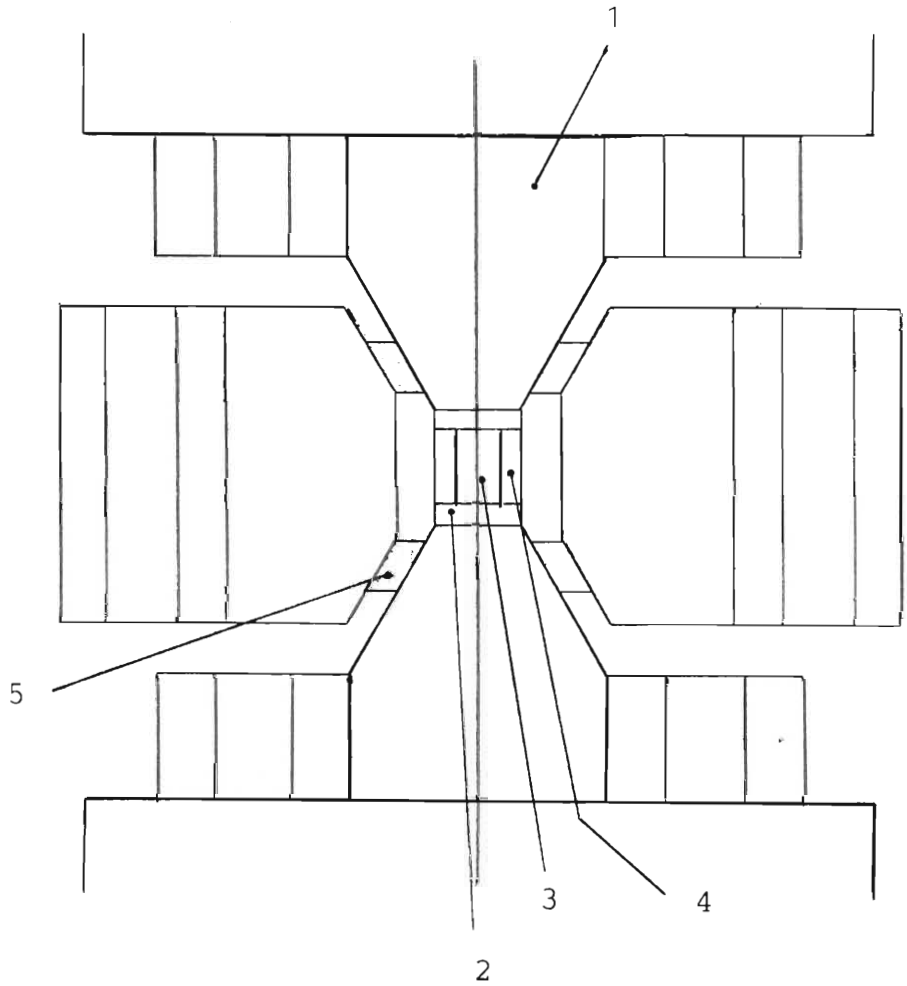

Figure 1.1 (a):A schematic section through a typical belt apparatus. 1,tungsten carbide anvil; 2,electrical contacts; 3,reaction volume; 4,heater sleeve; 5,gaskets [Fi79].

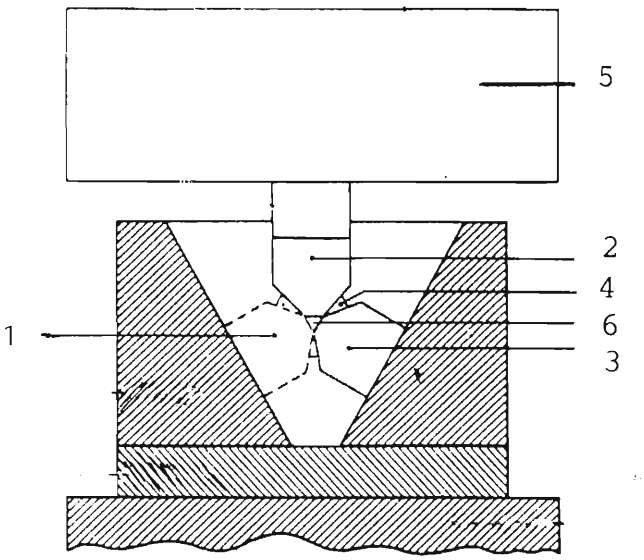

Figure 1.1 (b):A schematic section through a tetrahedral anvil apparatus:1,2,3, three of the four anvils; 4,gasket area; 5,press frame; 6,reaction volume [Fi79].

The exact nature of the diamonds produced in a synthesis experiment depends on the pressure and temperature cycle, the nature of the solvent, carbonaceous material and, lastly, the specific capsule design used.

The graphitization of carbons from partially graphitic carbon is significantly enhanced by pressure and the addition of transition metals, in particular the normal synthesis solvents, Ni, Co and Fe [De75]. The metal content of synthetics may range from several tenths of 1% by weight to several percent.

The process of diamond synthesis can be regarded to comprise of three stages, as illustrated below :

(i) carbon $\xrightarrow[\text{graphitization}]{\text{metal-catalytic}}$ graphite

(ii) graphite $\xrightarrow{\text{dissolution}}$ metal-carbon solution

(iii) metal-carbon solution $\xrightarrow[\text{growth}]{\text{nucleation}}$ diamond.

At each of the three stages the nature of the carbon-metal surface plays an important role. In order to fully graphitize the carbon and subsequently dissolve it in the metal, it is necessary for the metal to react with the carbon. Good wettability of molten metals with graphite and diamond indicates that the metals react chemically with the carbon to form carbides and solution in the metal.
The theories discussing the role of the solvent-catalyst can be categorised into three broad groups relating to the mechanism of diamond synthesis.

(i) <u>The pure catalyst approach</u>.

The key element in diamond synthesis is that the metal atoms diffuse between the graphite planes to form weakly bonded graphite intercalation compounds. The metal catalyst in this position promotes the structural re-arrangement of the starting graphite structure. Micro-crystals of these compounds go into

solution in the bulk molten metal and migrates to the growing surface.

(ii) The pure solvent approach

The graphite dissolves in the solvent until all its bonds are broken. Diamond then crystallizes from the melt from a super-saturated solution.

(iii) The solvent - catalyst approach

In this approach the metal catalyst acts as a solvent in which graphite readily dissolves. The dissolved carbon forms intermediate compounds that subsequently decompose to form diamonds. It is generally felt that such intermediate compounds are metal carbides. At present the solvent-catalyst approach is the dominant mechanism generally used in commercial diamond synthesis.

(2) Reconstitution technique

Good quality crystals have been grown by using this technique in which fine diamond powder is used as a starting material. This material is dissolved in the molten solvent, at pressures above the three-phase equilibrium point. A seed is placed in contact with the solvent, but at a lower temperature than the source diamond, so that carbon precipitates from the solution on to the seed.

(3) Shock wave synthesis

In these experiments a solid metal body containing small inclusions of graphite was shocked to pressures up to 140 GPa. When the metal was dissolved away, a residue of diamond remained. The metal, being less compressible, is only heated to 1800 K whereas the graphite, being more compressible has its volume collapsing to that of diamond. Shock wave diamonds may also be synthesized using an exponential focussing horn plus a magnetic hammer [Fi79].

(4) Epitaxial growth

Diamond has been grown onto a diamond substrate by Fick (1971). In these experiments carbon was sublimed onto a vacuum-cleaved diamond surface. An epitaxial layer of polycrystalline cubic and hexagonal diamond were formed [We79].

An alternative way of growing diamond-like layers on a clean diamond surface is to fire a low energy beam of carbon ions at its surface. These ions striking the carbon growth layer, have enough energy to break the weak chemical bonds between those carbon atoms bonded together in linear chains. Only the most strongly bonded atoms (diamond) survive in the growth layer. This technique is known as molecular beam epitaxial growth [We79].

(5) Vapour-liquid-solid (VLS) growth

Diamond has been grown by cracking methane on single crystal diamond substrates. In these experiments, a skin of solvent metal on the diamond was used as a transporting agent for the carbon source material. The solvent metals used were nickel, iron and manganese.

(6) Chemical Vapour Deposition (CVD) diamonds

The requirements for growing diamonds by this method are a hot diamond, whose surface is clean on the atomic scale, and a source of carbon atoms. There are basically four methods for the stable growth of CVD diamonds viz., plasma-assisted CVD, thermally assisted CVD, reactive vapour deposition and various combination of these [Ya90]. Eversole [We79], used a methyl group containing gas in which diamond growth was effected from a carbon containing vapour. When methane is used, the decomposition equilibrium is given as:

$$CH_4 \rightleftharpoons C \text{ (diamond or graphite)} + 2\,H_2 \,.$$

The substrate for diamond growth used is fine diamond powder and substrate temperatures in the range 1200-1400 K are preferred. Other gases which can be used in place of methane includes ethane, propane and methyl chloride.

Eversole, also described the growth of diamond using carbon monoxide.

$$2\ CO\ (g) \longrightarrow C\ (diamond) + CO_2$$

CVD diamonds can also be obtained by the following reaction:

$$C_2H_2 + 2\ H \longrightarrow C\ (diamond + graphite) + CH_4(g)$$

The graphite is then removed as follows:

$$C\ (graphite) + 4\ H \longrightarrow CH_4\ (g)$$

In the metastable synthesis of CVD diamonds at low pressures, an important invention to the reaction was the addition of atomic hydrogen. This eliminated the need for diamond substrates. This reaction is shown below :

$$CH_4 \xrightarrow[\text{atomic hydrogen}]{\text{heat \&}} C\ (diamond) + 2\ H_2\ .$$

Atomic hydrogen serves a number of critical roles in CVD diamond growth. One of them is the reduction of the size of the critical nucleus [An90].

1.4 HYPERFINE INTERACTION STUDIES OF DIAMOND

Several techniques have been used to investigate impurity sites and defects in diamonds. The nuclear methods, which detect hyperfine interactions by means of their influence on nuclear radiation, can be grouped into three classes: the Mössbauer Effect (ME), the perturbed angular correlation techniques (PAC) and the perturbed angular distribution methods (PAD).

1.4.1 PERTURBED GAMMA RAY ANGULAR DISTRIBUTION AND CORRELATION STUDIES IN DIAMOND AND OTHER CARBON ALLOTROPES.

In the PAD technique, a pulsed particle beam from an accelerator is directed onto a target placed perpendicular to the beam axis. The nuclear reaction excites the isomeric levels and simultaneously aligns the nuclear spins. The angular distributions of the gamma radiation(s) emitted from these aligned excited states are anisotropic for a nuclear spin $I \geq 1$. In the case of magnetic hyperfine interaction, the interaction of the nuclear magnetic moment with the hyperfine magnetic field results in a change of the m-state population.
This re-population is reflected in the angular distribution of the gamma radiation. The PAD method requires a nuclear reaction in order to produce the nuclear alignment needed for the observation of magnetic or electric hyper-

fine interactions. A second possibility of generating an alignment (PAC technique) is presented by the angular distribution of the radiation field itself, since this distribution depends in a well-known way on the nuclear spins, the m-sublevel population parameters, and the multipolarity of the radiation. Thus, the detection of gamma quanta in an arbitrary direction results in an alignment of the "observed nuclei". Any subsequent radiation emitted by the same nuclei shows a characteristic angular distribution with respect to the first radiation. In this method the nuclear level must be the intermediate level in the γ-γ cascade. The populating γ transition ("γ1") selects a sub ensemble with a defined alignment. The angular distribution of γ2 then reflects this sublevel [Ch83].

Appel et al.[Ap81], implanted ^{111}In ions into diamond. After applying Time Differential Perturbed Angular Correlation (TDPAC) techniques for different crystal orientations, it was found that a small fraction of the probe ions came to rest at characteristic lattice sites with well defined quadrupole interaction frequency ν_o = (117.8 ± 0.6) MHz. It was assumed that the rest of the of implanted ions occupied a variety of lattice sites. Analysis indicated that the ‹111› crystal directions were dominant as far as the axes of the electric field gradient (EFG) were concerned.

Raudies [Ra83] implanted ^{181}Hf at high temperatures into single crystal diamond. After annealing, residence site parameters were determined for the implanted ions from TDPAC measurements employing the $\gamma(133\ keV)-\gamma(482\ keV)$ cascade in ^{181}Ta.

A small fraction of the ions experienced an axially symmetric EFG $V_{zz}(1) = 5.5 \times 10^{17}\ V.cm^{-2}$ and $V_{zz}(2) = 9.6 \times 10^{17}\ V.cm^{-2}$, respectively. The bulk of the ions were strongly disturbed by higher EFG's with symmetries along the <111> crystal axes. Interstitial and substitutional tetrahedral sites were favoured as residence sites for the implanted ions.

The results obtained from ^{181}Hf studies agreed well with ^{111}In data and in both cases it was found that only a small fraction of the probe ions came to rest at characteristic lattice sites with well-defined quadrupole interaction frequencies and definite symmetries.

Studies using the TDPAD technique in diamond [Co90, S-H92] consistently revealed two unique residence sites for the recoil implanted ^{19}F in different types of natural diamonds.

These correspond to well defined quadrupole interaction frequency ν_{Q1} = 63(2) MHz and ν_{Q2} = 56(2) MHz. The first corresponds to the formation of a C-F bond at an intrabond

site and the second is interpreted as a distorted substitutional site. A third quadrupole interaction frequency ν_Q = 33(3) MHz was associated with a broadly distributed site with random efg orientation. It was suggested that this could indicate local amorphous conditions around the probe implants and was interpreted as arising from the formation of H-F molecular complexes [S-H92].

TDPAD analysis of ^{19}F implanted in carbon allotropes and graphite yielded two residence sites for the implants, with unique electric field gradients. The principal efg component for the ^{19}F implant sites has a quadrupole frequency of ν_Q = 57 MHz [Bh89]. This coupling frequency was in excellent agreement with those determined for the quadrupole interaction at the F site in CF_4. Together with the results from cluster calculations, it was suggested that this EFG component may be associated with the fairly undisturbed C-F bond. The results further indicate that the residence sites of ^{19}F in diamonds and carbon allotropes are locally very similar.

1.4.2 ^{57}Fe MÖSSBAUER STUDIES IN NATURAL DIAMOND

Results obtained from ^{57}Fe Mössbauer studies in natural diamonds may provide a better understanding of electric field gradients at iron inclusions sites in synthetic diamonds.

Temperature dependent measurements of ^{57}Co implanted into natural diamonds [Sa81] revealed the existence of two components in the Mössbauer spectra, a single line and a quadrupole-split doublet, with the single line contribution increasing strongly upon the annealing of the sample.

The single line component displayed a large isomer shift (δ = -0,95 mm.s^{-1}.) indicating an unusually large s-electron density at the iron nuclei and a high Debye temperature of the iron atoms, $\Theta_{eff} \approx$ 800 K [Sa81]. On this basis it was concluded that Fe atoms in regular high symmetry (HS) sites (substitutional or tetrahedral interstitial sites) in diamond are exposed to very high pressure and are highly restricted in their vibrational amplitudes.

The low-symmetry (LS) iron sites (characterized by a quadrupole-split doublet) indicated a high electric field gradient and are thought to be connected with damaged regions in the lattice as in the case of Si and Ge hosts.

Further investigations of the Mössbauer study of ^{57}Co implanted into heated natural diamonds revealed that the implantation process introduced substantial damage into the diamond matrix which causes almost all the implanted atoms to be situated in the disturbed lattice or a lattice with some degree of amorphisation. It was found that the best least square fits can be obtained by a single line

with an asymmetric doublet, with Lorentzian line shapes, but assuming equal areas for the two lines of the doublet [Sa83].

Sawicka et al.[Sa83], in their experiments concluded that the virtual absence of a temperature dependence for the intensity of the single line showed confirmation that the Debye-Waller factor and the effective Debye temperature for iron implants at cubic sites in diamond are very high ($f = 1$, $\Theta_D = 1000$ K).

Furthermore, for the quadrupole-split doublet a strong temperature dependence was observed below 100 K. This showed an anomalous rise of the recoil free fraction for low symmetry (LS) sites below 100 K [Sa90]. This effect was explained as due to localized jumps of interstitial impurity atoms between adjacent tetrahedral and hexagonal positions in the host lattice.

Recently, Sawicka et al.[Sa90] implanted Fe ions into diamond crystals which were heated to 830 K during implantation. About 20 % of the implanted ions were found to end up in high-symmetry (HS) sites, with the remaining 80% of the ions appearing in low-symmetry (LS) sites. The HS sites were characterized by very high Debye temperature of $\Theta_D \approx 1300$ K and by high s-electron density. The implants at LS sites exhibited a Debye temperature of 550 ± 50 K and a large EFG, viz., $V_{zz} = 1.2 \times 10^{18}$ V.cm^{-2}.

1.4.3 ^{57}Fe MÖSSBAUER STUDIES IN SYNTHETIC DIAMOND.

H. Armon et al.[Ar82] analysed the Mössbauer spectra of inclusions of Fe, Ni, Co or mixtures thereof in three commercially available diamond powders viz., CDA, MDAS and SDA. The spectra were substantially different, reflecting the different composition and synthesis conditions that characterized these three different samples. The SDA diamond powder showed a magnetically split spectra due to Fe in a specific ferromagnetic phase. The co-existence of a very small amount of Fe in a paramagnetic phase was also evident. The Mössbauer data were sensitive to stress exerted on the inclusions but for the CDA sample, the inclusions were stress free.

Karfunkel et al. [Ka85] made a systematic study of the differences in Mössbauer spectra for different diamond types viz., MDAS, CDA and SDA as well as the variations with grain size for each type. The Mössbauer spectra (for the MDAS samples) showed a collapse of the hyperfine structure to a broad singlet, in going from the coarser to finer grain sizes (250-63 μm). This was explained as due to superparamagnetism. Once the relaxation time becomes too short, fine single domain particles may, due to thermal agitation, get out of alignment with the resulting collapse of the magnetic field. They predicted that for suparamagnetism to occur, the critical size for the iron particles

must be of the order of ≈100 Å. They concluded that since the samples were mesh sorted, the larger crystals also permitted the growth of larger inclusions by diffusion of iron or aggregation.

For the CDA diamonds there was also evidence of collapse to the superparamagnetic state. In the most coarse fraction (250–177 μm), the singlet was already present and the six hyperfine lines were broad, of different widths and size compared to the MDAS diamond samples. It was also observed that as the grain size decreased, the singlet disappeared completely. They interpreted this as a very rapid crystallization in which iron was essentially not crystallized, viz., amorphous, or it was present in this form between diamond crystal grains.

A surprising result for the smallest grain (37–30 μm) was the re-appearance of the magnetic hyperfine structure as well as a doublet in the spectrum.

Maguire et al. [Ma86] employed a combination of rotational hysteresis measurements and ^{57}Fe Mössbauer spectroscopy over a temperature range up to 900 K in order to obtain information about the chemical nature and size distribution of iron inclusions in synthetic diamond. The Mössbauer spectra of three types of synthetic diamonds were analysed viz., Types CDA, SDA and MDAS. Type CDA synthetic diamond showed broadened magnetic splittings and a central singlet

at all temperatures from 78 K up. The intensity of the singlet increased with temperature and the mean magnetic field decreased as was to be expected for superparamagnetic fine particles. It was suggested that the broadening of the lines may be due to "diffusive inclusions" with an indeterminate boundary of a carbide or carbon alloy phase. The SDA material gave a well-defined magnetic sextuplet at 300 K with a superparamagnetic component.

Type MDAS diamond produced a simple magnetic spectrum at 300 K and no superparamagnetic component. The isomer shift data for the MDAS diamond displayed a non-linearity above 500 K indicating that ^{57}Fe are subjected to high pressures. The torque magnetometry results show that the metallic inclusions have a range of sizes up to $\approx$ 1000 Å.

1.5 PROJECT OBJECTIVES

The review of the relevant literature given above suggested several objectives for the present study of Fe inclusions in diamond using Mössbauer spectroscopy.
These are :

1. To determine the nature of the sites of the Fe inclusions, and to obtain information on Fe-C bonding from hyperfine interaction parameters describing the Mössbauer spectra.

2. To investigate systematically the variation with grain sizes of the hyperfine interactions at the Fe sites and therefore the physical conditions around the probe ions.

3. To study the probe-dependence of the electric field gradients in diamond.

2. PRINCIPLES OF MÖSSBAUER SPECTROSCOPY.

2.1 INTRODUCTION

The phenomenon of the emission or absorption of a gamma-ray photon without the loss of energy due to recoil of the nucleus is known as the Mössbauer Effect. It was discovered by Rudolph Mössbauer in 1957 and is of fundamental importance in that it provided a means of measuring some of the comparatively weak interactions between the nucleus and the surrounding electrons.

The interdisciplinary nature of this technique and its numerous applications are illustrative both of the ways in which science develops and how it leads to technological advancement.

Mössbauer Spectroscopy has grown rapidly to one of the most important research methods in solid-state physics, chemistry, metallurgy and biology.

The Mössbauer Effect began to be widely applied to chemical and mineralogical research after it was shown in 1960 that ^{57}Fe exhibited this resonant phenomenon.

2.2 THE MÖSSBAUER EFFECT

To gain insight into the physical basis of the Mössbauer Effect and the importance of recoilless emission of γ-rays, a variety of factors must be considered. These are :-

2.2.1 Energetics of free-atom recoil and thermal broadening.

2.2.2 Heisenberg natural line width.

2.2.3 Energy transfer to the lattice.

2.2.4 Recoil-free fraction.

2.2.1 ENERGETICS OF FREE-ATOM RECOIL AND THERMAL BROADENING

Consider an isolated atom in the gaseous phase and define the energy difference between the ground state of the nucleus (E_g) and its excited state (E_e) as (see Figure 2.1)

$$E_o = E_e - E_g.$$

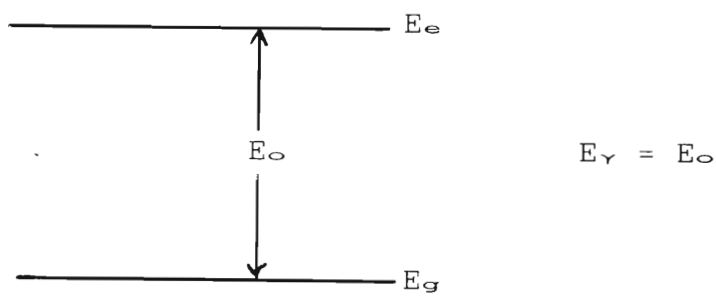

Figure 2.1 : Energy difference between the ground state of the nucleus (E_g) and its excited state (E_e) as $E_o = E_e - E_g$.

If the photon is emitted from a nucleus of mass M moving with initial velocity V_x in the x-direction, (see Figure 2.2), then its total energy is $(E_o + \frac{1}{2} MV^2_x)$. After emission the γ-ray will have an energy E_γ and the nucleus has a new velocity $(V_x + v)$ due to recoil (note that v is a vector quantity so that its direction can be opposite to V_x). The total energy of the system is $E_\gamma + \frac{1}{2} M (V_x + v)^2$.

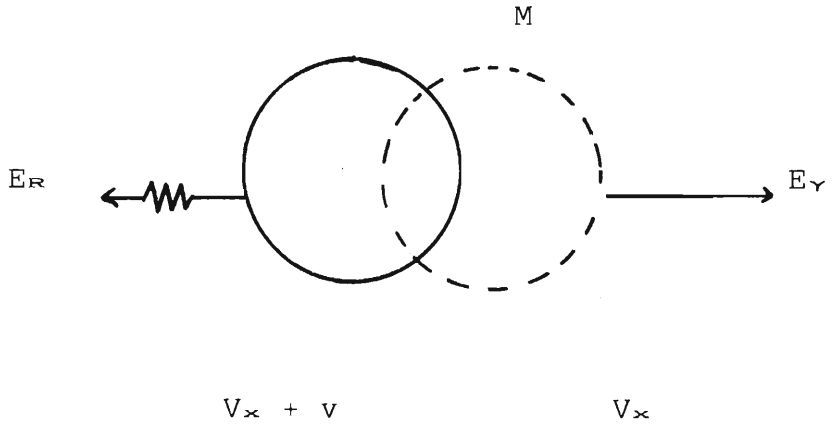

Figure 2.2 : Emission of a gamma ray of energy E_γ from an excited nuclear state of a nucleus having a velocity V_x. E_R is the recoil energy, and $E_o = E_e - E_g$ [Ba73].

From conservation of energy,

$$E_o + \tfrac{1}{2} MV^2_x = E_\gamma + \tfrac{1}{2} M (V_x + v)^2$$

The difference between the energy of the nuclear transition (E_o) and the energy of the γ-ray photon (E_γ) is

$$\delta E = E_o - E_\gamma = \tfrac{1}{2} Mv^2 + MvV_x \qquad (2.1)$$

$$= E_R + E_D \qquad (2.2)$$

From equation (2.1) and (2.2), $E_o > E_\gamma$. Thus the γ-ray energy is seen to differ from the nuclear energy level separation by an amount which depends on the recoil energy ($E_R = \tfrac{1}{2} Mv^2$) as well as the Doppler-effect energy ($E_D = MvV_x$).

The recoil energy can be expressed as :

$$E_R = \tfrac{1}{2} Mv^2 = (Mv)^2/2M = p^2/2M$$

where p is the recoil momentum of the nucleus. Since momentum must be conserved, this will be equal and opposite to the momentum of the γ-ray photon, p_γ,

$$p = -p_\gamma = -E_\gamma/c$$

hence $$E_R = E^2_\gamma/2Mc^2$$

E_R results in a shift of the photon energy and the Doppler term, E_D being dependent on the velocity of the emitting atom, results in the thermal broadening of the line. Thus referring to equation 2.2, the γ-ray distribution is

displaced by E_R and broadened by twice the geometric mean of the recoil energy and the average thermal energy i.e., E_D The distribution itself is Gaussian and is shown in Figure 2.3.

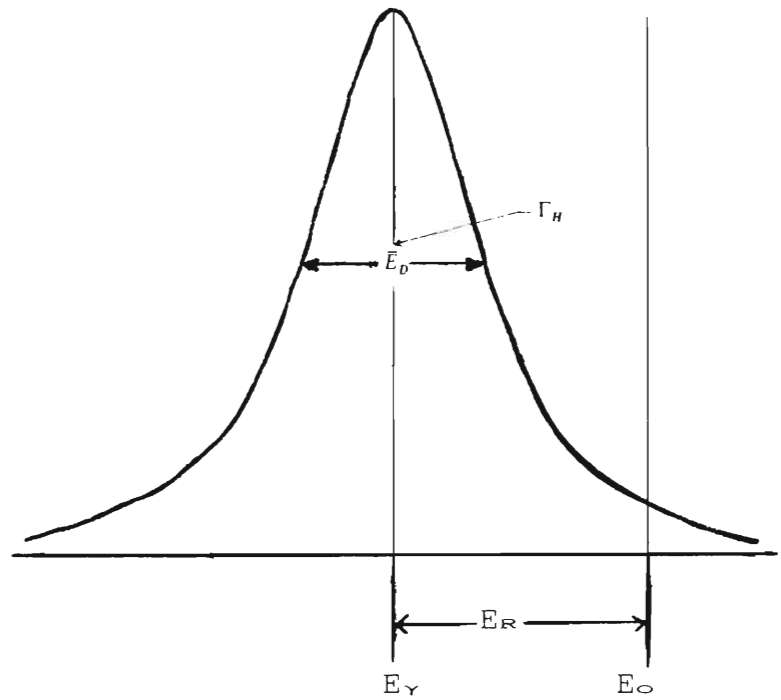

Figure 2.3 : The statistical energy distribution of the emitted γ-ray showing the interrelationship of E_γ, E_o, E_R and E_D [Ba73].

The emitted γ-ray has energy $E_\gamma = E_o - E_R$. For resonance absorption to occur, the γ-ray must have energy $E_\gamma' = E_o + E_R$ (conservation of energy). As a result, the maxima of the emission and absorption lines are removed from each other by a distance 2 E_R (see Figure 2.4), and if 2 $E_R \gg \Gamma$, where Γ

is the natural width of γ-line, resonance fluorescence cannot occur. If $E_R < \Gamma$, the recoil has practically no influence on the effect of resonance absorption.

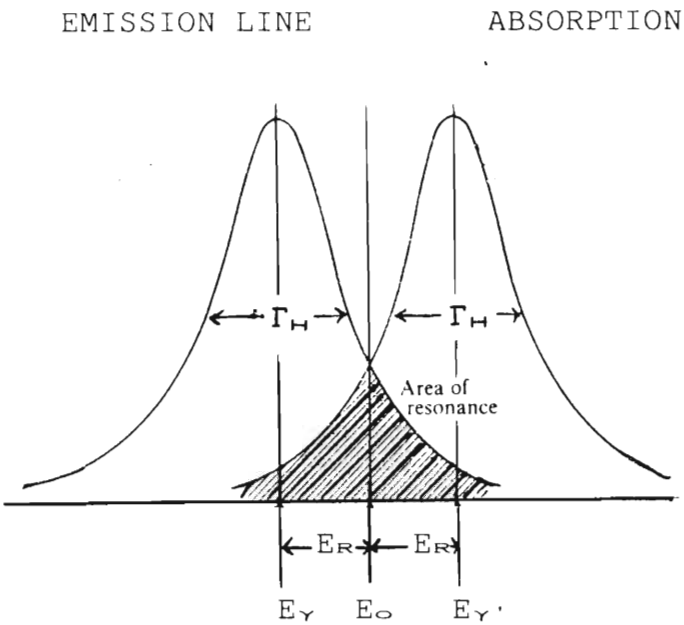

Figure 2.4 : The resonance overlap of emission and absorption spectra. The area of resonance is shaded [Ba73].

2.2.2 HEISENBERG NATURAL LINEWIDTH.

One of the most important influences on a γ-ray energy distribution is the mean lifetime of the excited state. The uncertainties in energy and time are related to Planck's constant by the Heisenberg Uncertainty Principle

$$\Delta E \, \Delta t \geq \hbar$$

The excited state of the source has a mean life τ of a microsecond or less, so that there will be a spread of γ-ray energy of width Γ_H at half height where

$$\Gamma_H \tau = \hbar \quad , \quad \tau = t_{\frac{1}{2}}/\ln 2$$

For ^{57}Fe, the half-life of the "Mössbauer" state at 14.4 keV is $t_{\frac{1}{2}}$ = 97.7 ns and $\Gamma_H = 4.67 \times 10^{-9}$ eV.
Thus the line width is infinitesimal compared to E_γ.

2.2.3 ENERGY TRANSFER TO THE LATTICE.

In 1957 Mössbauer discovered that a nucleus in a solid matrix can sometimes emit and absorb gamma-rays without recoil because in a solid the nucleus is no longer isolated, but is fixed within the lattice. Under favourable conditions the gamma-rays may be emitted without any loss of energy due to the recoil of the nucleus.

Mössbauer reasoned that for some low energy gamma rays, E_R and E_D became negligible such that the emission and absorption energy profiles overlapped completely and line widths approaching Γ_H were observed, resulting in a resonance spectrum.

Consider an emitting nucleus that is not rigidly bound, but is free to vibrate. The recoil energy could be transferred to the lattice by increasing the vibrational energy of the crystal, particularly as the two energies are of the same order of magnitude. The vibrational energy levels of

the crystal are quantised and can only change by discrete amounts in integral multiples of $\hbar\omega$. Thus, unless the recoil energy of the nucleus corresponds closely with one of the allowed discrete increments it cannot be transferred to the lattice, thus ensuring that the whole crystal recoils, leading to negligible recoil energy.

Again E_R and E_D become minute and $E_o \approx E_\gamma$, and resonance is easily observable.

2.2.4 RECOIL-FREE FRACTION.

Because E_R and lattice excitation energies are of comparable magnitude, only a certain fraction of the emissions and absorptions take place without recoil, and this fraction will vary from solid to solid, as well as decreasing as E_γ (and thus E_R) increase. This fraction f is known as the Mössbauer recoiless fraction, and is given by [Gr71]

$$f = \exp\left[\frac{-4\pi^2 \langle x^2 \rangle}{\lambda^2}\right]$$

where :

λ is the wavelength of the gamma photon, and $\langle x^2 \rangle$ is the mean square vibrational amplitude of the emitting (or absorbing) nucleus in the solid.

For any real crystal the recoilless fraction f will always be smaller than unity and to increase the relative strength of the recoilless resonant process f must be as large as possible. The larger λ becomes (the small E_γ), the larger f becomes : In ^{57}Fe, E_γ = 14.4 keV resulting in a large f factor. It is observed that recoilless emission or absorption is optimized for a low energy γ-ray with a nucleus strongly bound in a crystal lattice at low temperature.

2.3 THE MÖSSBAUER SPECTRUM

The source of γ-rays is a radioactive nucleus which is incorporated into a host which is chosen such that energy levels to the probe nucleus remain unsplit. Identical nuclei in the absorber then act as probes of the electric and magnetic fields and electric field gradients in their vicinity.

The intensity of the γ-radiation transmitted through the absorber is measured as a function of velocity v (i.e., the effective γ-ray energy). This yields the characteristic Mössbauer absorption spectrum (see Figure 2.9). The effective E_γ value can be altered by moving the source and absorber relative to each other with a velocity v. Due to the Doppler shift the effective E_γ differs from the energy $E_{\gamma o}$ value by an amount $\varepsilon = (v/c)\, E_{\gamma o}$. When the effective E_γ values are exactly matched to the energy difference between the ground state and excited state (multiplets) of the probe nucleus in the absorber resonance absorption occurs.

The excited absorber nuclei re-emit the γ-ray within $\sim 10^{-7}$s. If the internal conversion coefficient is high, fewer γ-rays will be emitted. More significantly, the re-emission is not directional but takes place over the full 4π solid angle. Consequently the number of secondary events recorded at the detector are few and usually negligible. In transmission geometry, the γ-detector thus shows resonance dips in the count rate at source velocities at which resonance absorption has occurred.

2.4 HYPERFINE INTERACTIONS.

A Mössbauer spectrum is characterized by the number, shape, position and relative intensity of the various absorption lines.

The peak positions in a Mössbauer spectrum are sensitive to the extranuclear environment, such that different compounds give different spectra. The differences in spectra can be attributed to the so called hyperfine interactions i.e., the interactions between the nuclear charge distribution and the extranuclear electric and magnetic fields. These hyperfine interactions give rise to the isomer shift (I.S.), and the quadrupole splitting (Q.S.) and the magnetic hyperfine splitting of the energy levels of the probe nuclei.

The following sections will consider the various hyperfine interactions and briefly discuss how these relate to the types of information that can be obtained from Mössbauer Spectroscopy.

2.4.1 THE ISOMER SHIFT.

The isomer shift manifests itself as a shift from zero velocity of the centroid of the Mössbauer resonance spectrum and is due to the electrostatic interaction between the charge distribution of the nucleus and that of those electrons which have a non-vanishing probability in the

region occupied by the nucleus.

The nucleus has a finite volume and during γ-transition, it is usual for the effective nuclear size to alter, thereby changing the nucleus-electron interaction energy. This change is only a minute fraction of the total Coulombic interaction which is dependent on the chemical environment. This energy change is obtained by comparing values obtained from a suitable reference spectrum (eg., ^{57}Fe source-natural iron absorber spectrum).

The nucleus is assumed to be a uniformly charged sphere of radius R, and the s-electron density at the nucleus, $[\psi(o)_s]^2$, is assumed to be a constant over the nuclear dimensions. The difference in energy between the electrostatic interaction of a point nucleus with $[\psi(o)_s]^2$, and the interaction of a nucleus having a radius R with $[\psi(o)_s]^2$ is given by

$$\delta E = K[\psi(o)_s]^2 R^2$$

where K is the nuclear constant.

Since R is different for ground and excited nuclear states, δE will be correspondingly different for both (see Figure 2.5) and is given by

$$\delta E = \delta E_e - \delta E_g = K[\psi(o)_s]^2 [R_e^2 - R_g^2]$$

where the R_e is the radius of the excited state and R_g is the radius of the ground state.

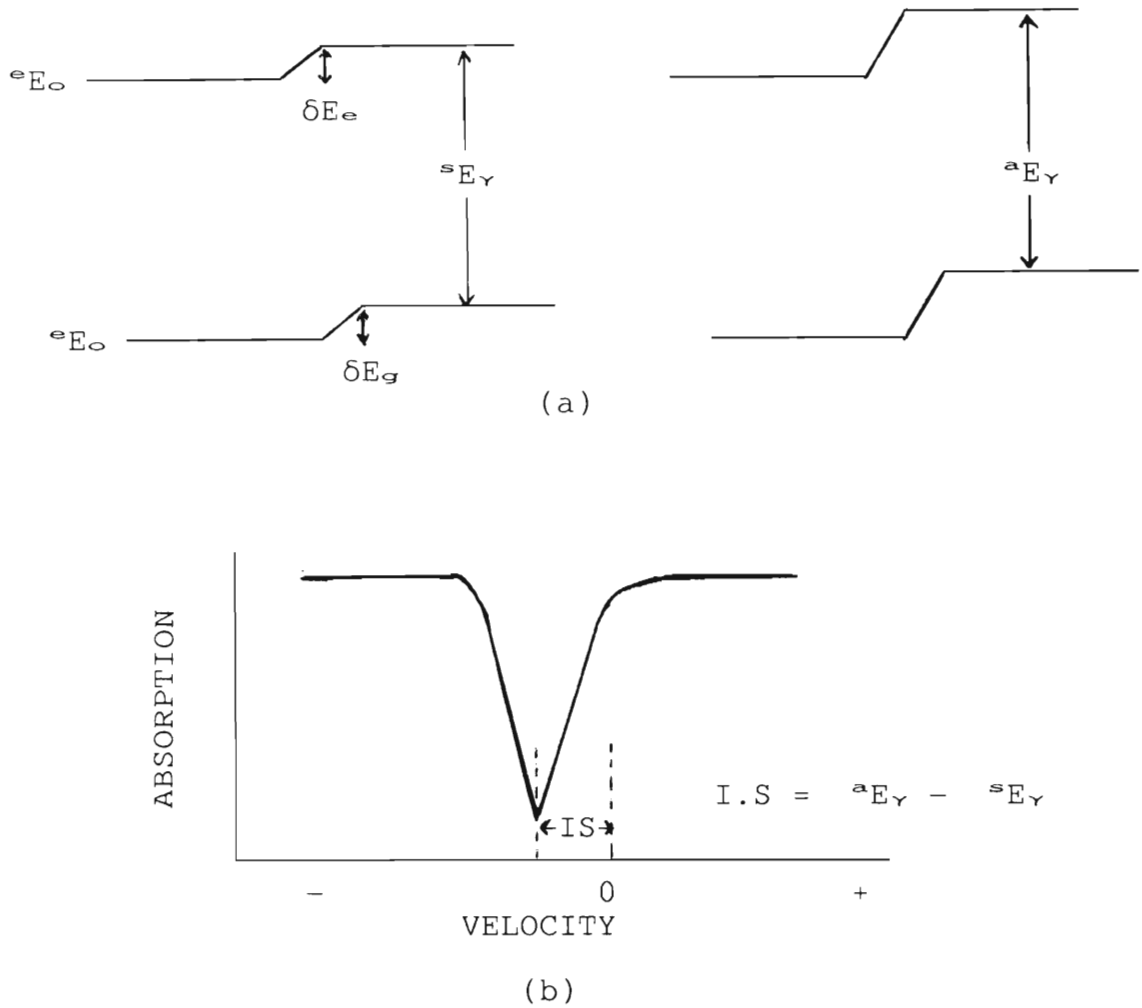

Figure 2.5: Nuclear energy levels and the isomer shift

(a) Source and absorber nuclear energy levels,

(b) Isomer Shift observed in a Mössbauer spectrum.

The isomer shift, δ, as measured in a Mössbauer experiment is the difference in energy between two chemical environments A and B and is given by [Gr71]

$$\delta = \frac{4}{5}\pi Z e^2 \{ |\psi_s(0)_A|^2 - |\psi_s(0)_B|^2 \} R^2 \delta R/R$$

where the term in brackets is the difference in electron charge density at the nuclear site between the source and the absorber and $\delta R = R_{ex} - R_{gd}$ is the difference in radius of the excited and ground states. The isomer shift thus allows us to determine the nuclear radius and the total charge density at the nucleus.

If $\delta R/R$ is positive (as for ^{119}Sn), this implies an increase in the s-electron density at the absorber nucleus, resulting in positive isomer shift. If $\delta R/R$ is negative (as for ^{57}Fe), an increase in the s-electron density at the absorber nucleus results in a more negative isomer shift.

If the sign of $\delta R/R$ is known, the isomer shift provides a qualitative method of examining the covalent character of a bond or bonds involving a Mössbauer isotope and a potential method for determining the valency and oxidation state of the Mössbauer atom.

It is also of interest to note that isomer shift of energy levels can also arise from the thermal motion of the Mössbauer atoms. This is known as the second order Doppler

effect. It is usually much smaller than the isomer shift and can often be ignored for similar compounds at the same temperature.

2.4.2 THE ELECTRIC QUADRUPOLE INTERACTION

In Section 2.4.1, it was assumed that the nuclear charge distribution was spherical. However, nuclei in states with spin $I > \frac{1}{2}$ have non-spherical charge distributions which are characterized by a nuclear quadrupole moment Q. The nuclear quadrupole moment reflects the deviation of the nucleus from spherical symmetry and is expressed by [Gi76]

$$e\,Q = \int \rho r^2 \,(3\cos^2\theta - 1)\, d\tau \quad .$$

where +e is the charge on the proton, and ρ is the charge density in the volume element $d\tau$ at a distance r from the center of the nucleus at an angle θ to the axis of the nuclear spin. Q is positive if the nucleus is prolate and negative if it is oblate in shape.

In an non-isotropic electric field, i.e., one with an electric field gradient, the nuclear quadrupole moment experiences an electric quadrupole interaction, which results in a precession of the quadrupole moment about the principal axis of the EFG, and gives rise to a splitting of the nuclear energy levels.

The spin Hamiltonian which describes the nuclear quadrupole interaction can be written as

$$\mathcal{H} = \frac{eQ}{2I(2I-1)}\left(V_{zz}I_z^2 + V_{yy}I_y^2 + V_{xx}I_x^2\right) \qquad (2.3)$$

where -e is the charge of the electron, Q is the nuclear quadrupole moment, I is the nuclear spin, I_j is the projection of I on the j axis, V is the electric potential, and $-V_{ij} = -(\partial^2 V/\partial x_i x_j)$ is the ith component of the electric field gradient (EFG) tensor in the principal axis system (x, y, z). Since the electric field is a vector, the gradient operator produces a symmetric 3 x 3 second-rank tensor which can be diagonalized in the principal axis system and completely specified by V_{xx}, V_{yy} and V_{zz}.
In the region of the nucleus only s electrons have a spherically symmetric distribution and do not contribute to the EFG [Ko84]. Laplace's equation requires the EFG to be a traceless tensor, i.e.,

$$V_{xx} + V_{yy} + V_{zz} = 0$$

so that only two independent parameters are needed to specify an arbitrary EFG. It is conventional to specify the EFG in terms of a quantity q defined by $V_{zz} = eq$ and an asymmetry parameter η defined as

$$\eta = \frac{V_{yy} - V_{xx}}{V_{zz}}$$

such that $|V_{zz}| \geq |V_{yy}| \geq |V_{xx}|$, and $0 \leq \eta \leq 1$ [Gi76]. For axial symmetry $V_{xx} = V_{yy}$ and $\eta = 0$.

The Hamiltonian, given by equation (2.3), can then be written in terms of the two independent quantities q and η as

$$\mathcal{H} = \frac{e^2qQ}{4I(2I-1)} [3 I_z^2 - I(I + 1) + (I_x^2 - I_y^2)]$$

The ground state of ^{57}Fe has $I = \frac{1}{2}$ which precludes a quadrupole interaction. The 14.4 keV level has $I = 3/2$, and a quadrupole moment $Q \neq 0$.

Thus the presence of an EFG leads to a splitting of this state into two levels characterized by $m_e = \pm 1/2$ and $m_e = \pm 3/2$ (Figure 2.6 (a)) separated in energy by [Gi76]

$$E_Q = \pm \frac{e^2qQ}{2} (1 + \eta^2/3)^{\frac{1}{2}} \qquad (2.4)$$

which is the peak separation observed in a quadrupole-split spectrum of ^{57}Fe (as shown in Figure 2.6 (b)). In equation (2.4) eQ is the nuclear constant, and eq is a function of the chemical environment of the probe nucleus.

A measurement of the quadrupole splitting from the above equation (2.4) can result in information about the magnitude of q and η, and the sign of the quadrupole splitting.

The quadrupole splitting ΔE (see Figure 2.6) obtained from the Mössbauer spectrum involves both a nuclear quantity, the quadrupole moment (Q), and the electric field gradient, a property of the electron distribution around

the probe nucleus. The value of Q is fixed for a given nuclide and thus the details of the EFG can be obtained.

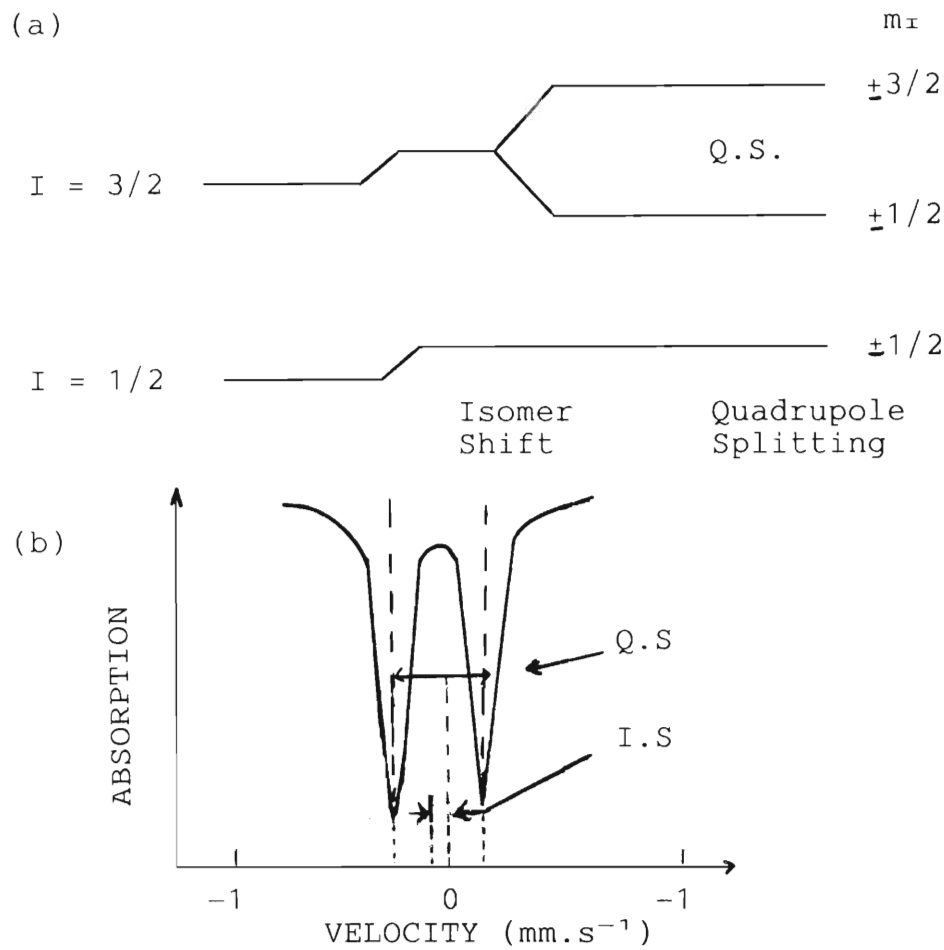

Figure 2.6: Nuclear energy levels and the quadrupole splitting.

(a) Absorber energy levels:excited level(I=3/2) split into two by quadrupole interaction,

(b) resultant Mössbauer spectrum [Ba73].

The effective EFG is the result of a number of different contributions viz.,

(i) the asymmetry of electronic structure as a result of the valence electrons of the Mössbauer atom,

(ii) the asymmetry in the lattice, and

(iii) molecular orbitals.

The effects of these contributions at the Mössbauer nucleus are modified by the polarization of the core electrons of the Mössbauer atom which may suppress or enhance the EFG. Thus the quadrupole splitting reflects the symmetry of the bonding environment and the nature of local structure in the vicinity of the Mössbauer atom. It can give information relating to semiconductor properties, defects in solids etc.

2.4.3 THE MAGNETIC DIPOLE INTERACTION

When a nucleus is placed in a magnetic field there is a magnetic dipole interaction between the nuclear magnetic moment and the effective magnetic field, H, at the nucleus.

The magnetic field can originate within the atom itself, within the crystal via exchange interactions, or as a result of placing the compound in a externally applied magnetic field.

The Hamiltonian describing the magnetic dipole hyperfine interaction is [Gr71]

$$\mathcal{H} = - \mu.H = -g\mu_N \, I.H$$

where μ_N is the nuclear magneton ($e\hbar/2Mc$), μ is the nuclear magnetic moment, I is the nuclear spin, and g is the nuclear g factor.

The matrix elements are evaluated from the spin operator form of equation (2.5) and result in eigenvalues of

$$E_m = \frac{-\mu m H}{I} = -g\mu_N \, m_I H \qquad (2.5)$$

where m_I is the magnetic quantum number representing the z component of I (i.e., m_I = I, I-1, .., -(I-1), -I). The magnetic field splits the nuclear level of the spin I into (2 I + 1) equi-spaced substates.

The Mössbauer transition can take place between two different nuclear levels if the change in m_I value is 0, ± 1 or in some cases ± 2. The allowed transitions for a 3/2 ⟶ 1/2 Mössbauer ^{57}Fe γ-ray are illustrated in Figure 2.7 giving rise to a six-line spectrum which is symmetrical about the centroid.

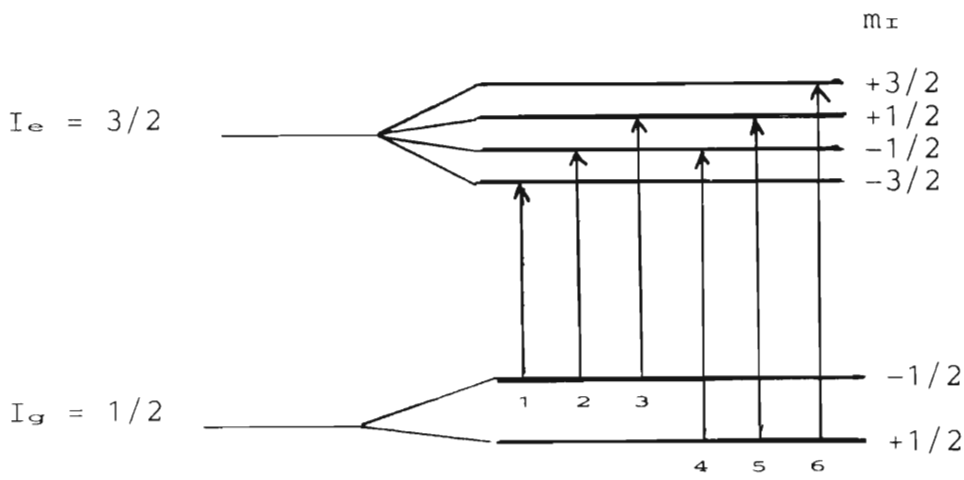

Figure 2.7: The magnetic splitting of an $I_g = 1/2 \rightarrow I_e = 3/2$ transition in ^{57}Fe showing the absorption transitions [Di86].

2.4.4 COMBINED MAGNETIC AND QUADRUPOLE INTERACTIONS.

Both the magnetic and quadrupole hyperfine interactions express a directional interaction of the nucleus with its environment but when present together their principal axes are not necessarily co-linear, and the interpretation of the Mössbauer spectrum can be quite complex.

For the 1/2 $\longrightarrow$ 3/2 transition, and provided $e^2qQ \ll \mu H$, the quadrupole interaction can be treated as a first-order perturbation to the magnetic interaction.

The resultant energy levels are given by [Gr71]

$$E_{QM} = -g\mu_N H.m_I + (-1)^{|m_I| + \frac{1}{2}} 1/8(e^2qQ)\ (3\cos^2\Theta - 1)$$

where Θ is the angle between the magnetic axis and the major axis of the electric field tensor. All the magnetic hyperfine lines are shifted (Figure 2.8) by a quantity [Gi76]

$$|\varepsilon| = 1/8\ (e^2qQ)\ (3\cos^2\Theta - 1)$$

but the angle Θ and the value of e^2qQ cannot be determined separately from the line positions. The presence of a small quadrupole perturbation is easily visible because the spectrum is no longer symmetrical about the centroid.

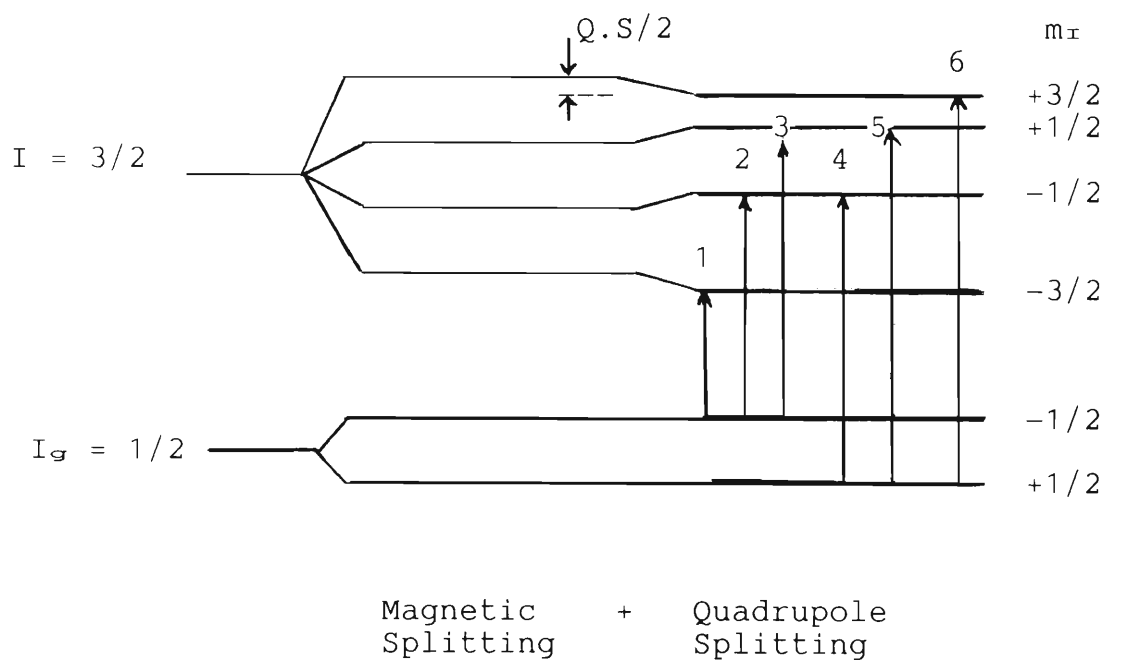

Figure 2.8: Energy level diagram for the combined magnetic and quadrupole splitting in ^{57}Fe [Gi76].

2.4.5 RELATIVE INTENSITY OF LINES

The individual lines in a spectrum (Figure 2.9) showing a hyperfine interaction have characteristics intensities which can be used to identify particular transitions. To determine the orientation of the magnetic axis EFG tensor in an anisotropic sample a detailed knowledge of the relative intensities of the absorption lines is necessary.

The intensity of particular hyperfine transition between quantized sub-levels is determined by the coupling of the two nuclear angular momentum states which can be expressed as the product of an angular dependent term and angular independent term. The angular independent term which corresponds to a case where there is no preferred orientation will be examined first.

The intensity in this case is given by the square of the appropriate Clebsch-Gordan coefficient [Gi76].

$$\text{Intensity} \propto |\langle I_1 L - m_1 m | I_2 m_2 \rangle|^2$$

where the two nuclear spin states I_1, and I_2 have I_z values of m_1 and m_2, and their coupling obeys the vector sums $L = I_1 + I_2$ and $m = m_1 - m_2$. L is referred to as the multipolarity of the transition, and the smaller values of L gives larger intensities.

The majority of Mössbauer isotopes have ground/excited state spins which are one of the following :
0, 2; 1/2, 3/2; 3/2, 5/2; 5/2,5/2; or 5/2, 7/2.
The ^{57}Fe absorption spectrum results from a 1/2+ $\longrightarrow$ 3/2+ M1 transition, and the Clebsch-Gordan coefficients are given in Table 2.1 [Gi76].

In a magnetically split spectrum there are eight possible transitions between levels and these levels are described by the m_1 and m_2 quantum numbers. The transitions +3/2 $\longrightarrow$ -1/2 and -3/2 $\longrightarrow$ +1/2 have zero probability (forbidden). The six finite coefficients, the squares of which are normalized (C^2) to give integral values of 3 : 2 : 1 : 1 : 2 : 3 intensity ratio for a magnetic hyperfine splitting (as shown in Figure 2.9). The corresponding terms for a quadrupole spectrum are obtained by summation and give a 1 : 1 ratio.

The angular dependent terms, $\Theta(L,m)$, (Table 2.1) are expressed as the radiation probability in a direction at an angle Θ to the quantization axis (i.e., the magnetic field axis or V_{zz}). The expected line intensity can be predicted from Table 2.1 to be in the ratios 3 : x : 1 : 1 : x : 3 where $x = 4 \sin^2\Theta/(1 + \cos^2\Theta)$ [Gi76].

An orientated absorber with a 3/2 $\longrightarrow$ 1/2 decay will have zero intensity in the m = 0 lines at $\Theta = 90°$ and a maximum intensity at $\Theta = 0°$.

Table 2.1 : The relative probabilities for a 1/2, 3/2 transition [Gr71].

Magnetic spectra(M1) m_2	$-m_1$	m	C (1)	C^2 (2)	C^2 (3)	$\Theta(L,m)$ (2)
+3/2	+1/2	+1	1	1/4	3	$3/4(1 + \cos^2\Theta)$
+1/2	+1/2	0	$\sqrt{(2/3)}$	1/6	2	$3/2 \sin^2\Theta$
−1/2	+1/2	−1	$\sqrt{(1/3)}$	1/12	1	$3/4(1 + \cos^2\Theta)$
−3/2	+1/2	−2	0	0	0	−
+3/2	−1/2	+2	0	0	0	−
+1/2	−1/2	+1	$\sqrt{(1/3)}$	1/12	1	$3/4(1 + \cos^2\Theta)$
−1/2	−1/2	0	$\sqrt{(2/3)}$	1/6	2	$3/2 \sin^2\Theta$
−3/2	−1/2	−1	1	1/4	3	$3/4(1 + \cos^2\Theta)$

Quadrupole spectra(M1) Transition	C^2 (2)	C^2 (3)	$\Theta(L,m)$ (2)
±1/2, ±1/2	1/2	1	$1/2 + 3/4 \sin^2\Theta$
±3/2, ±1/2	1/2	1	$3/4(1 + \cos^2\Theta)$

(1) The Clebsch-Gordan coefficient $\langle 1/2\ 1\ -m_1 m | 3/2\ m_2 \rangle$

(2) C^2 and $\Theta(L,m)$ are the angular-independent and angular-dependent terms normalized to a total radiation probability of $\sum_{m_1 m_2} C^2\ \Theta(L,m) = 1$

(3) C^2 arbitrarily normalized.

The equivalent behaviour in the quadrupole spectrum is a 1:3 ratio for the γ-ray axis parallel to the direction of V_{zz} and a 5:3 ratio perpendicular to V_{zz}.

If there are combined magnetic and quadrupole interactions, or the asymmetry parameter is non-zero, then in these circumstances the energy states are represented as a linear combination of terms.

The intensity is obtained by an amplitude summation to allow for interference effects.

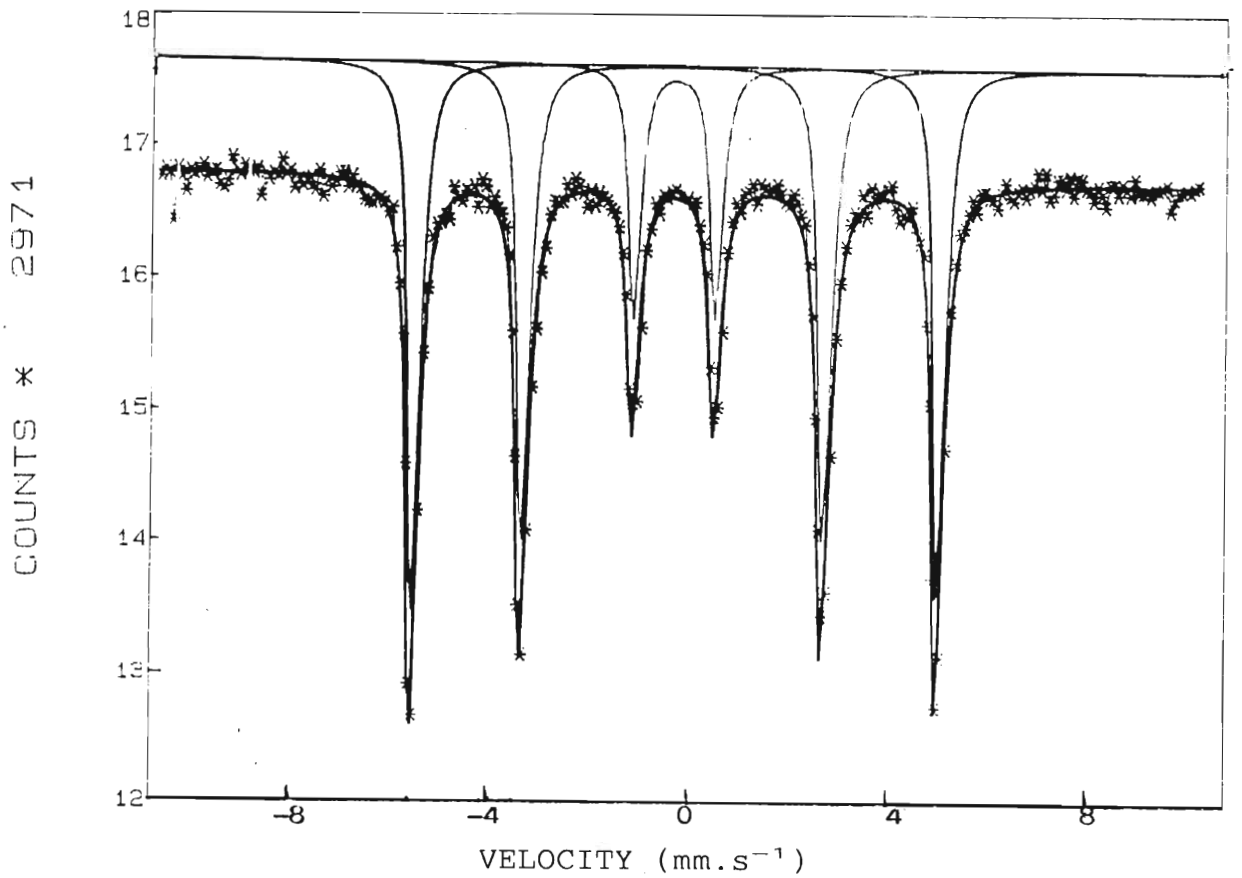

Figure 2.9 : A typical Mössbauer spectrum with an ^{57}Fe source and a natural iron absorber showing a sextet of lines with intensities in the ratio 3 : 2 : 1 : 1: 2 : 3.

3. EXPERIMENTAL DETAILS

3.1 MÖSSBAUER SPECTROMETER

The Mössbauer spectrum is a record of the counting rate of the appropriate γ-radiation emitted by a source and passing through (or scattered by) an absorber as a function of the instantaneous Doppler motion of the source/absorber system. It is therefore simply a record of transmission/absorption of γ-rays as a function of the energy of the incident radiation.

Central to the operation of a Mössbauer spectrometer is the introduction of a known and precise energy shift between emitter and absorber. This is achieved by introducing a relative motion between the source and absorber, which results in a Doppler shift in the energy of the γ-ray. The motion of the source is oscillatory in order to provide a scan over a selected energy interval.

A velocity sweep spectrometer is used in which the velocity range from $-v_{max}$ to $+v_{max}$ is continuously swept through with a frequency typically between 1 Hz and 100 Hz.

A typical spectrometer comprises of an electromechanical drive system, a detector system and the data acquisition system (multichannel analyser), and is illustrated in Figure 3.1

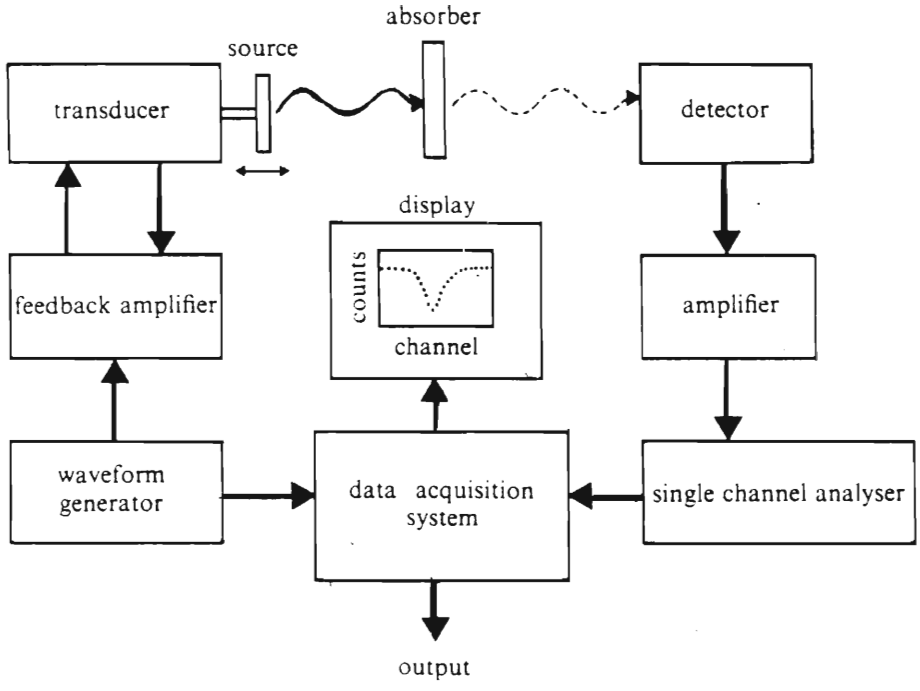

FIGURE 3.1 A block diagram of a Mössbauer spectrometer [Di86].

3.1.1 THE DETECTION SYSTEM

After a nucleus has been excited by recoilless absorption of Mössbauer γ-rays it decays to the ground state by emitting either γ-rays or internal conversion electrons, and in the latter case X-rays. The energy of the X-rays encountered in Mössbauer studies varies from about 3.4 keV to 200 keV and therefore different types of nuclear radiation counters are needed to detect these radiations.

The three main types of counters for detecting low-energy transitions (14.41 keV for ^{57}Fe) are :

(i) thin window NaI(Tl) scintillation counters
(ii) gas filled proportional counters and
(iii) Ge(Li) solid state counters.

In the present study, the detector used was a Reuter Stokes proportional counter filled with Kr-CO_2 gas mixture at 1 atmosphere. Proportional counters have much better resolution, higher signal to noise ratio for the low energy gamma rays, and negligible efficiency for the high energy γ-rays that might be present in the decay and contribute to the background [Go68].

The geometric arrangement of the source, absorber and detector is important since a γ-ray emitted along the axis of motion of the source has a Doppler shift relative to the absorber of $E_\gamma(v/c)$, but any γ-ray which travels to the detector along a path at an angle θ to this axis has an effective Doppler shift only $E_\gamma(v/c)\cos\theta$ [Gi76]. This causes a spread in the apparent Doppler energy of the γ-rays and hence line broadening. This effect can be reduced by maintaining an adequate separation between the source and detector.

3.1.2 THE SOURCE

In the case of an ^{57}Fe source, it is formed by electron capture of ^{57}Co with a half-life of $t_{\frac{1}{2}}$ = 270 days.
The reaction is represented as :

$$^{57}_{27}Co + e_{K} \longrightarrow {}^{57}_{26}Fe^{*} + \gamma + \bar{\nu}$$

In this reaction the interaction of an excited nucleus and the extranuclear electrons results in an electron capture accompanied by γ-ray emission together with a monoenergetic neutrino. A suitable source has to fulfil several factors if there is to be an easily observable Mössbauer resonance [Gi76]:

(1) The energy of the γ-ray must be between 10 to 150 keV, preferably less than 50 keV.

(2) The half-life of the first excited state which determines the natural linewidth Γ should be between about 1 and 100 ns.

(3) The internal conversion coefficient should be small (<10) so that there is a good probability of detecting the γ-ray.

(4) The ground state isotope should be stable and have a high natural abundance.

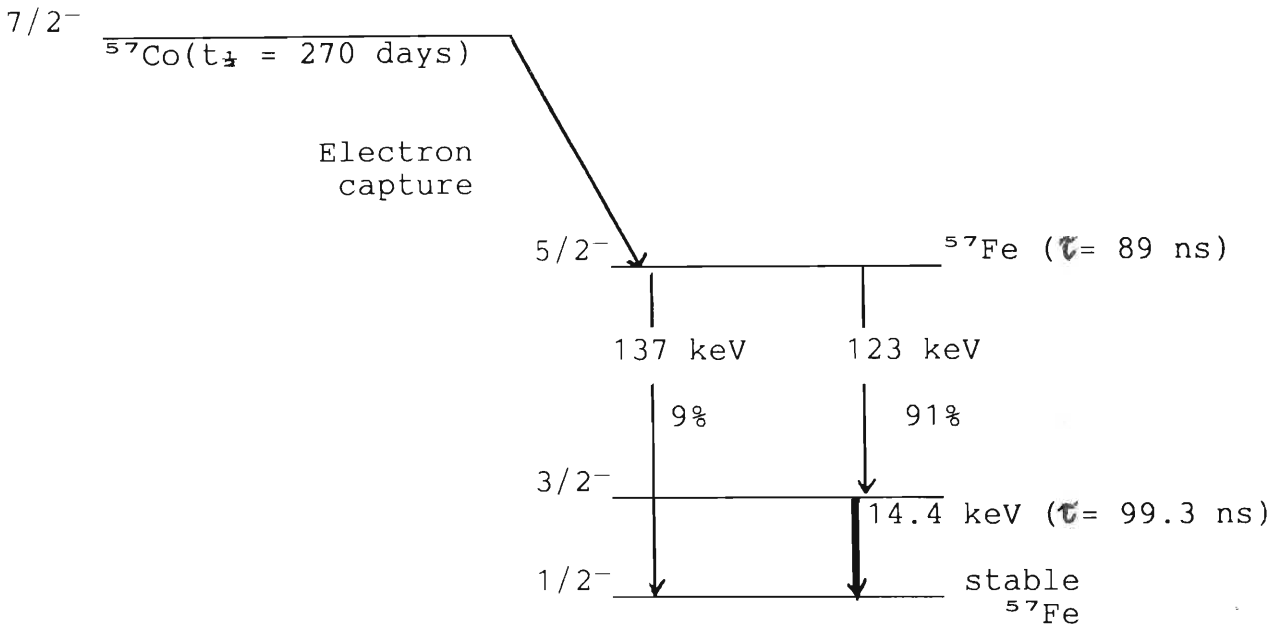

FIGURE 3.2 : The decay of ^{57}Co to stable ^{57}Fe.

For the present study the γ-transition in ^{57}Fe was appropriate and was obtained from a source of 10 mCi ^{57}Co in a rhodium matrix. The decay scheme is illustrated in Figure 3.2.

The long lived ^{57}Co nucleus decays by electron-capture with a half-life of 270 days to the 137 keV level of ^{57}Fe, which then gamma decays with a 85% branch to the 14.4 keV state The 14.4 keV transition occurs, without change in parity, between the excited state of spin 3/2 and a ground state of spin 1/2, and the transition is primarily of M1 type.
The half-life of this state is 99.3 ns, giving it a natural width of 4.7×10^{-12} MeV and a Heisenberg width of $\Gamma_r = 0.192$ mms^{-1} in the Mössbauer resonance [Gi76].

The large value of the internal conversion coefficient for this level reduces the source efficiency to less than 10% but the γ-ray is well resolved from the two higher γ-rays and the 7-keV X-rays produced by internal conversion. Although the natural abundance of ^{57}Fe is only 2.19%, the absorption cross-section of $\sigma_o = 2.57 \times 10^{-18}$ cm^3 is large, and results in a satisfactory resonance at room temperature [Gi76].

The radioactive source nuclei are usually embedded in a matrix which provides the necessary solid environment. One of the important experimental aspects is in the choice of a source matrix. Since the source has to be free of hyperfine interactions, ^{57}Co was diffused into a rhodium metal which was chosen as the host matrix.

3.1.3 THE ELECTROMECHANICAL DRIVE SYSTEM

The electromechanical drive system must be synchronized with the multichannel analyser so that the velocity changes linearly only from $- v_{max}$ to $+ v_{max}$ with increasing channel number. In this way the source is always moving at the same velocity when a given channel is open.

The driving system used in the present study consists of the electromagnetic Mössbauer Velocity Transducer (WISSEL) MVT-1000 and the Mössbauer Driving Unit (WISSEL) MDU-1000. It provides a precise motion of the γ-source

relative to the absorber during the Mössbauer effect measurements combined with the precise determination of the tranducer's velocity.

The Drive Unit feeds the Velocity Tranducer with an electronically controlled voltage. The Digital Function Generator Model DFG 1000 is used to provide the Mössbauer Driving systems with the reference signal which determines the waveforms of the source motion.

A waveform, with a voltage increasing linearly with time (see Figure 3.3), imparts a motion with a constant acceleration in which the drive shaft and the source spend equal time intervals at each velocity increment.

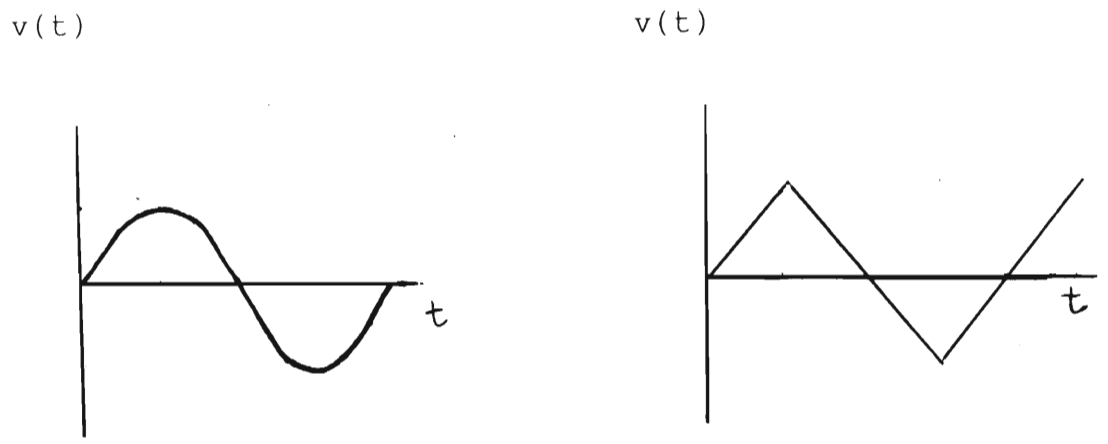

(a) sine wave (b) triangular wave

FIGURE 3.3: Typical waveforms used as reference signals for electromechanical tranducers.

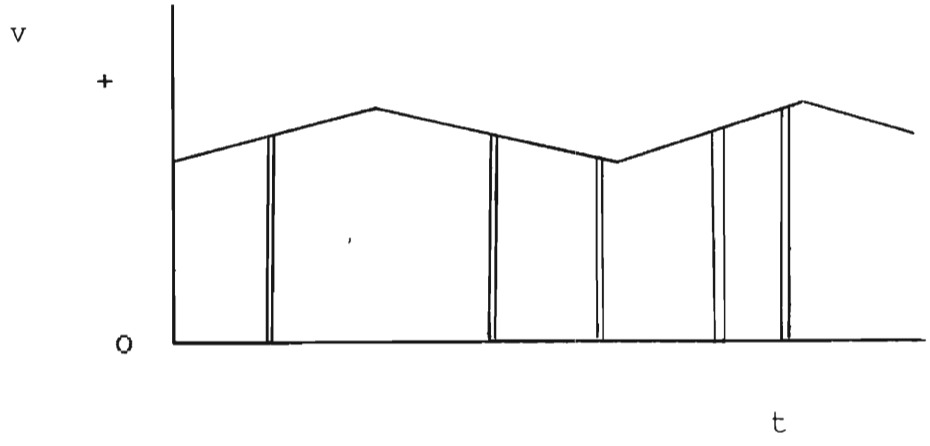

FIGURE 3.3(c): Each γ-ray can be used to produce a pulse with amplitude characteristic of the instantaneous velocity.

The Mössbauer Velocity Transducer embodies two mechanically coupled loudspeaker systems. The driving coil causes the motion of the drive shaft in the transducer (see Figure 3.4). The pick up coil feeds the information of the actual velocity back to the driving unit (MDU). Also compared by the MDU is the reference signal from the digital function generator (DFG). The feed-back system, formed in this manner, provides a source motion, with minimised deviation from its correct value.

One of the disadvantages of constant acceleration motion is that because of the symmetric nature of the motion executed by the driven shaft, the Doppler velocities which are obtained change from plus to minus and then from minus to plus during a single cycle. Since the data in the first half should be identical to that in the second half, one can accumulate information over the whole cycle and then "fold" the spectrum at the appropriate point. The disadvantage of this mode of operation lies in the fact that the 'folding point' must be determined with precision and must remain constant during the spectrum accumulation.

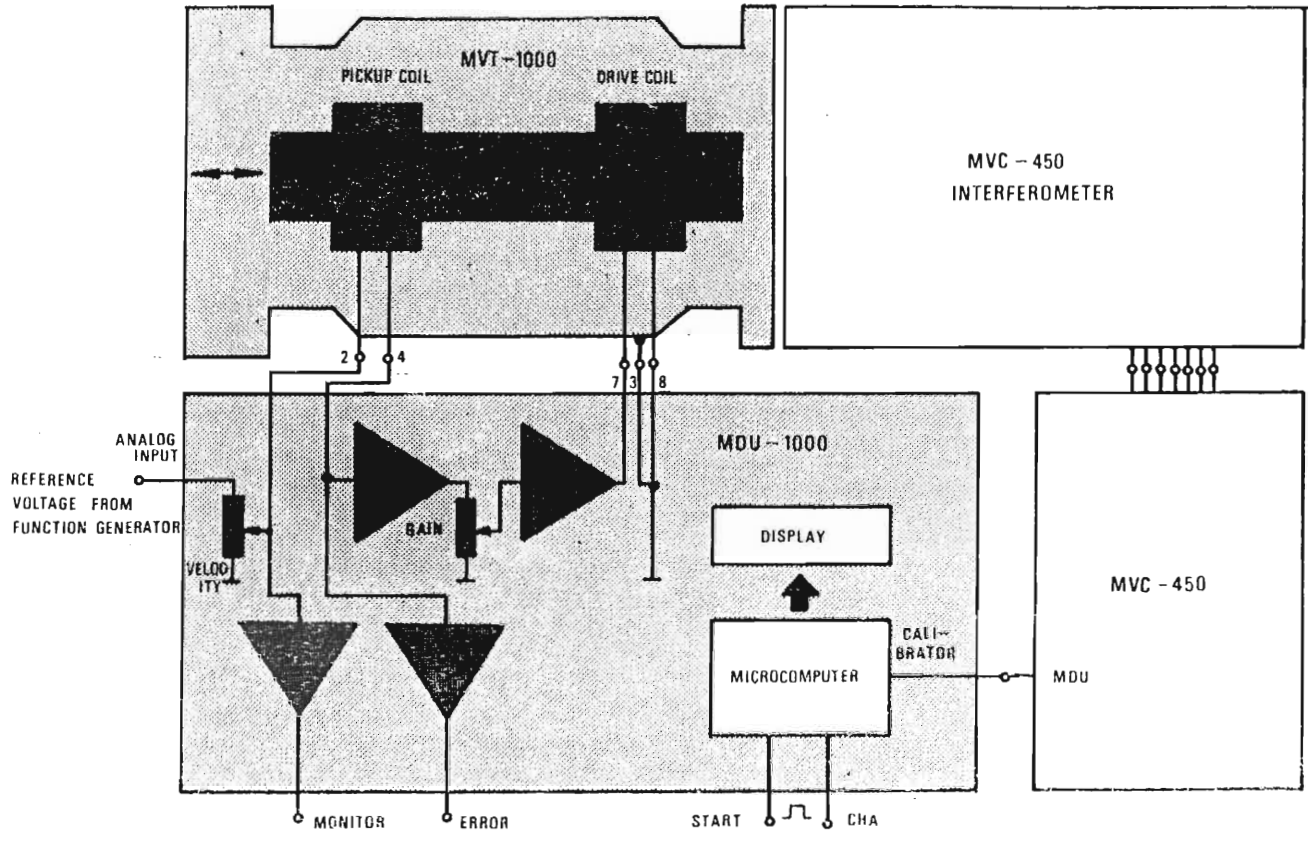

FIGURE 3.4 : A schematic representation of the WISSEL Driving System 1000.

Figure 3.5 shows a pulse height spectrum (PHA) obtained with a ^{57}Fe source and a Kr-CO_2 gas filled proportional counter. Each radioisotope produces a characteristic and readily identifiable spectrum of this type. The vertical column represents the number of counts tallied per channel while for the horizontal column, each channel represents a voltage interval.

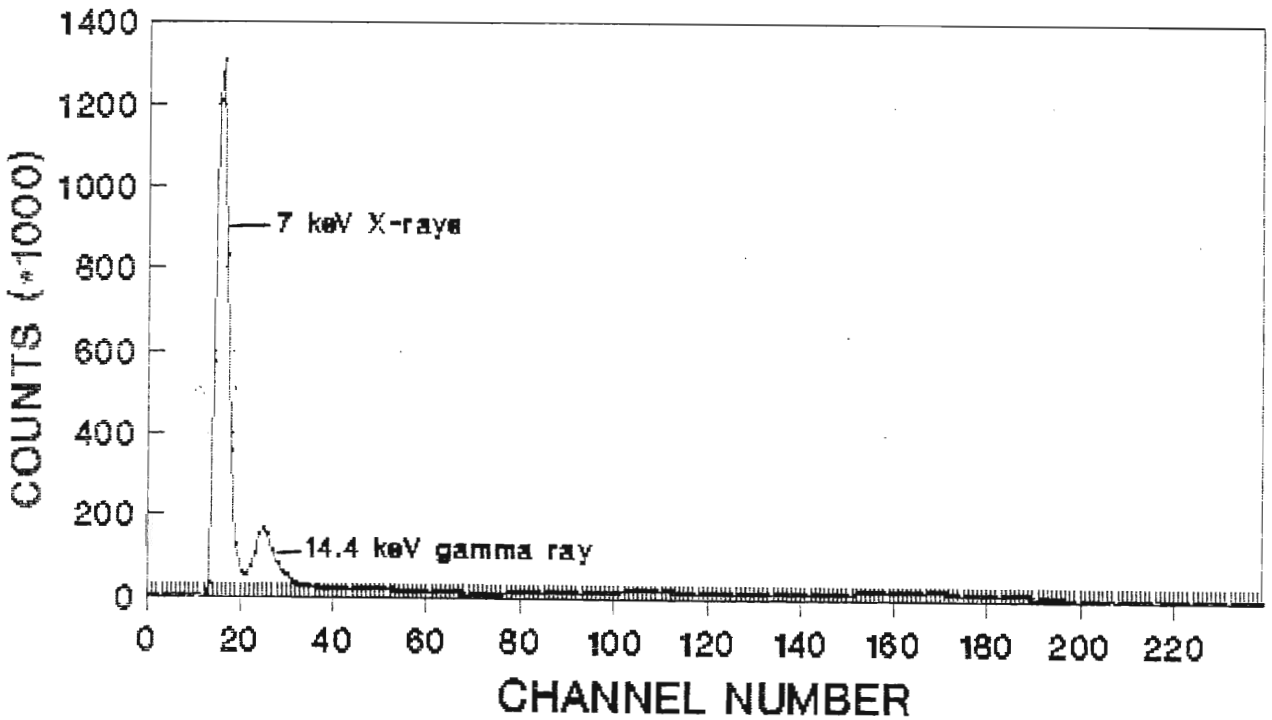

FIGURE 3.5: Pulse Height Analysis (PHA) spectrum of a ^{57}Fe obtained with a Kr-CO_2 proportional counter.

3.1.4 THE MULTICHANNEL ANALYSER

The multichannel analyser (MCA) stores an accumulated total of γ-counts in registers known as channels by using binary memory storage. It can perform data acquisitions in two basic modes i.e., Pulse Height Analysis (PHA) and Multi-channel scaling (MCS).

MCS analysis is used to obtain histograms representing frequency of occurrence vs. elapsed time. The input signal is a train of pulses, each of which represents a single event. There is no information contained in the amplitude or width of these pulses i.e., they are "logic" pulses in the sense that the occurrence of a pulse signals an event. MCS operation effectively employs the data memory as a series of scalers (pulse counters).

The multichannel scaling mode may be used with interval trigger or with the MCS scan synchronized to an external device. The channels of the MCS spectrum are then directly related to a position or condition of the external apparatus.

When used with a Mössbauer spectrometer the MCA (TN-7200) and the electromechanical drive system (WISSEL Series 1000 Drive System) are synchronized to maintain a linear velocity change from - v to + v with increasing channel number.

The spectrum is accumulated for a period typically of the order of hours or days during which time this spectrum is

monitored on a display screen. When a spectrum with a satisfactory signal-to-noise ratio has been obtained it is then stored on a disc for subsequent computer analysis.

Figure 3.6 represents a MCS spectrum where each point in the spectral trace represents the total number of counts accumulated during a time interval.

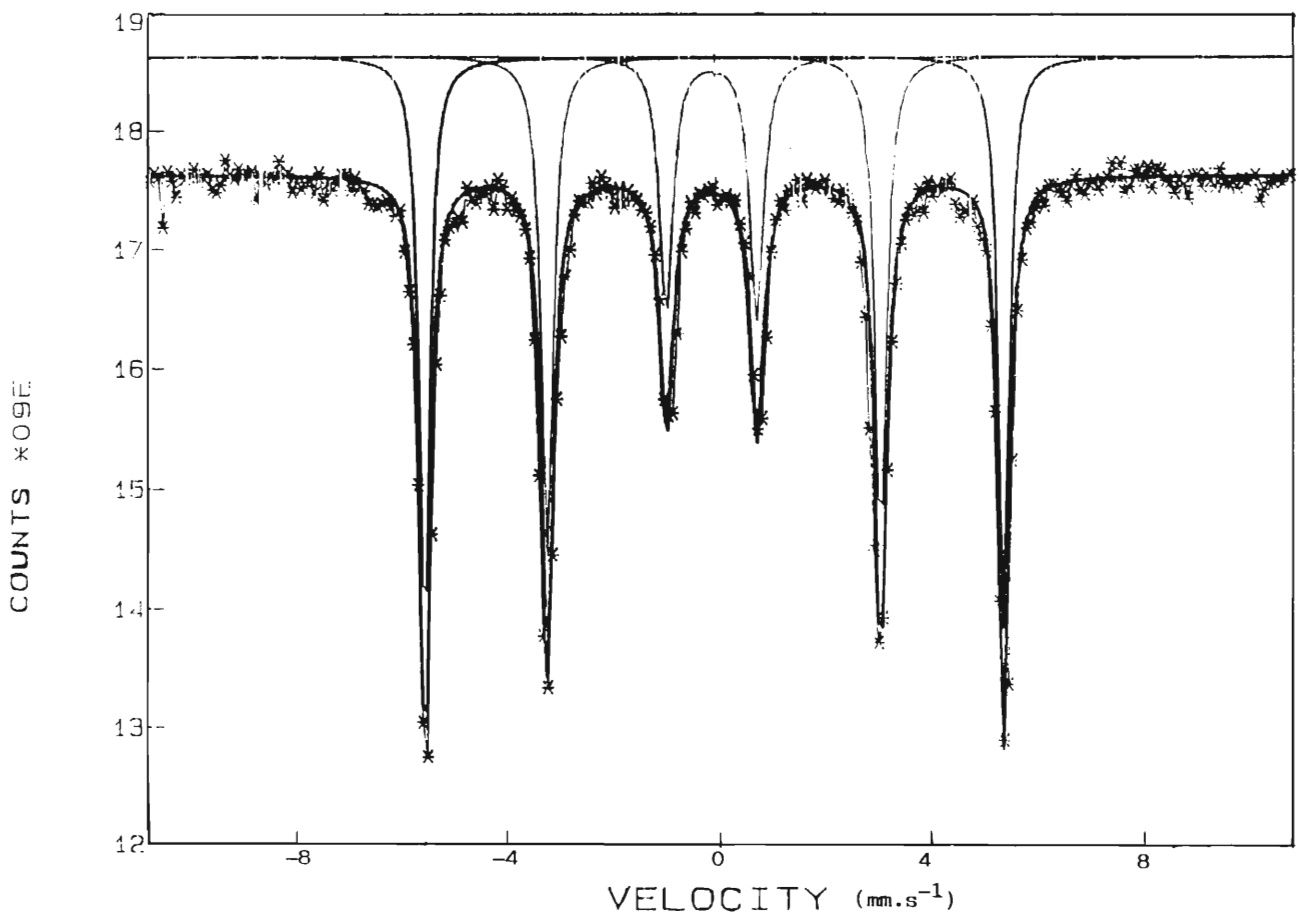

FIGURE 3.6 : The Mössbauer spectrum of ^{57}Fe in a 25 μm thick natural iron foil absorber recorded with a ^{57}Co (Rh source at room temperature.

4. SPECTRA AND ANALYSIS

4.1 THE MÖSSBAUER SPECTRA

The Mössbauer spectra of ^{57}Fe in a natural iron foil as shown in Figure 3.6, represents a simple example of a pure nuclear Zeeman effect. Because of the cubic symmetry of the iron lattice, there is no quadrupole shift of the nuclear energy levels. Since the intensity ratios for magnetically hyperfine split lines is in the ratio 3 : 2 : 1 : 1 : 2 : 3, the magnetic domains and, consequently the internal fields are randomly orientated and the radiation is unpolarised. S.S.Hanna et al. gave the first interpretation of the ^{57}Fe spectrum and showed that the hyperfine field at 300 K was H_{eff} = -33.3 T [Ha60]. Saegusa et al. [Sa82] also showed that the hyperfine field for α-Fe foil was H_{hf} = 33.04 T and that it has a body centred cubic (bcc) structure.

The Mössbauer spectra obtained in the present study for the different grain sizes of diamond are shown in Figure 4 (a) to Figure 4 (e). The samples with the largest grain size of 180-250 μm gave a well defined six component magnetically split spectrum (Figure 4 (a)). This was almost identical to the Zeeman split sextet lines obtained for natural iron (Figure 3.6). A 7th small peak was also observed near the centre of the spectrum.

On going to the smaller diamond grains (Figure 4 (b) to Figure 4 (d) the intensity of the magnetically split spectrum becomes greatly reduced and the central single line component increases rapidly in intensity. The spectra are dominated by this central single line (paramagnetic component) with an appearance of a weak asymmetric doublet for grain sizes in the range 45-105 μm.

A unique and unexpected observation for the finest grain size 38-25 μm, (mesh 400/500), is the reappearance of the six magnetic hyperfine splitting components together with the strong central single line paramagnetic component (Figure 4 (e)). The intensity of lines 1,2,5 and 6 of the magnetically split spectra is somewhat diminished when compared to the 180-250 μm diamond sample.

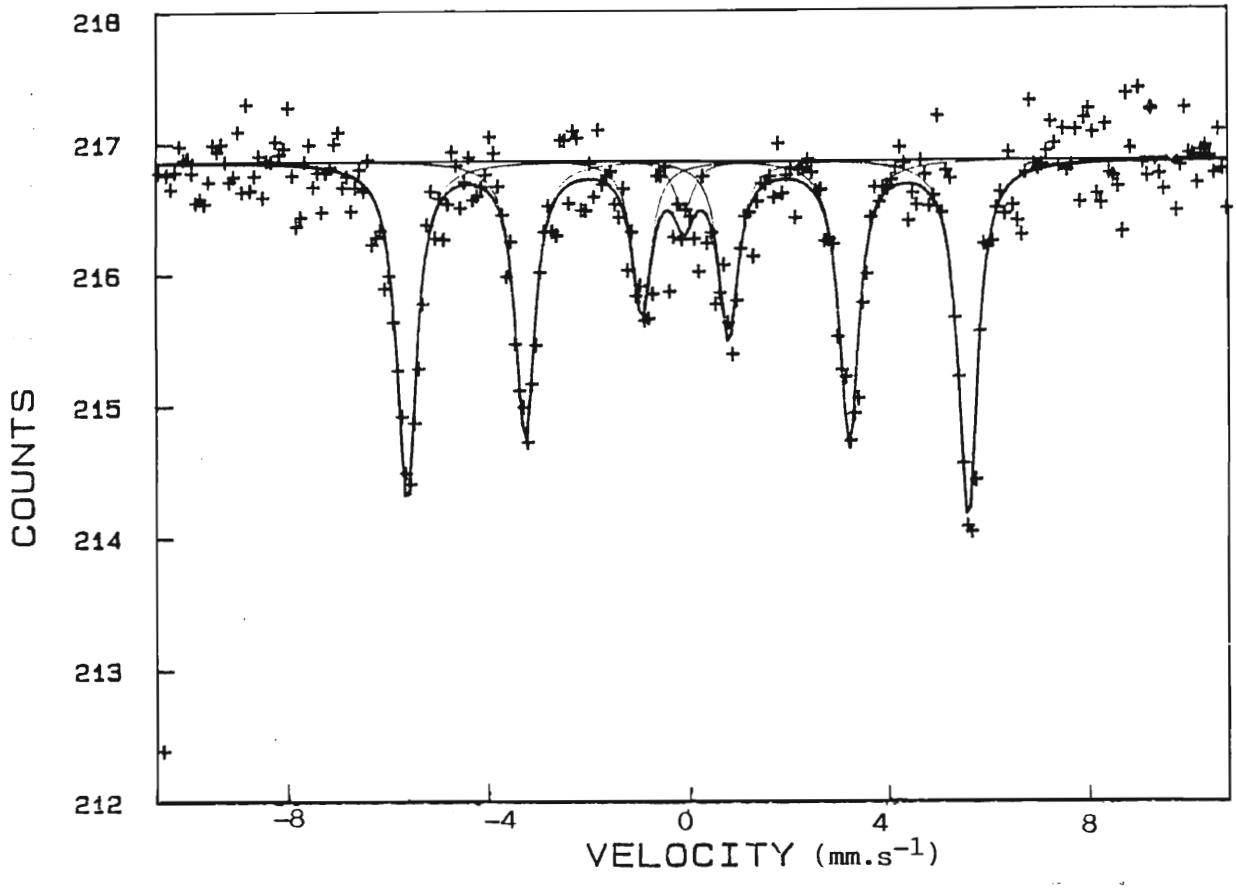

FIGURE 4 (a): ^{57}Fe Mössbauer spectrum for synthetic MDAS diamonds of grain size 250–180 μm (mesh 60/80).

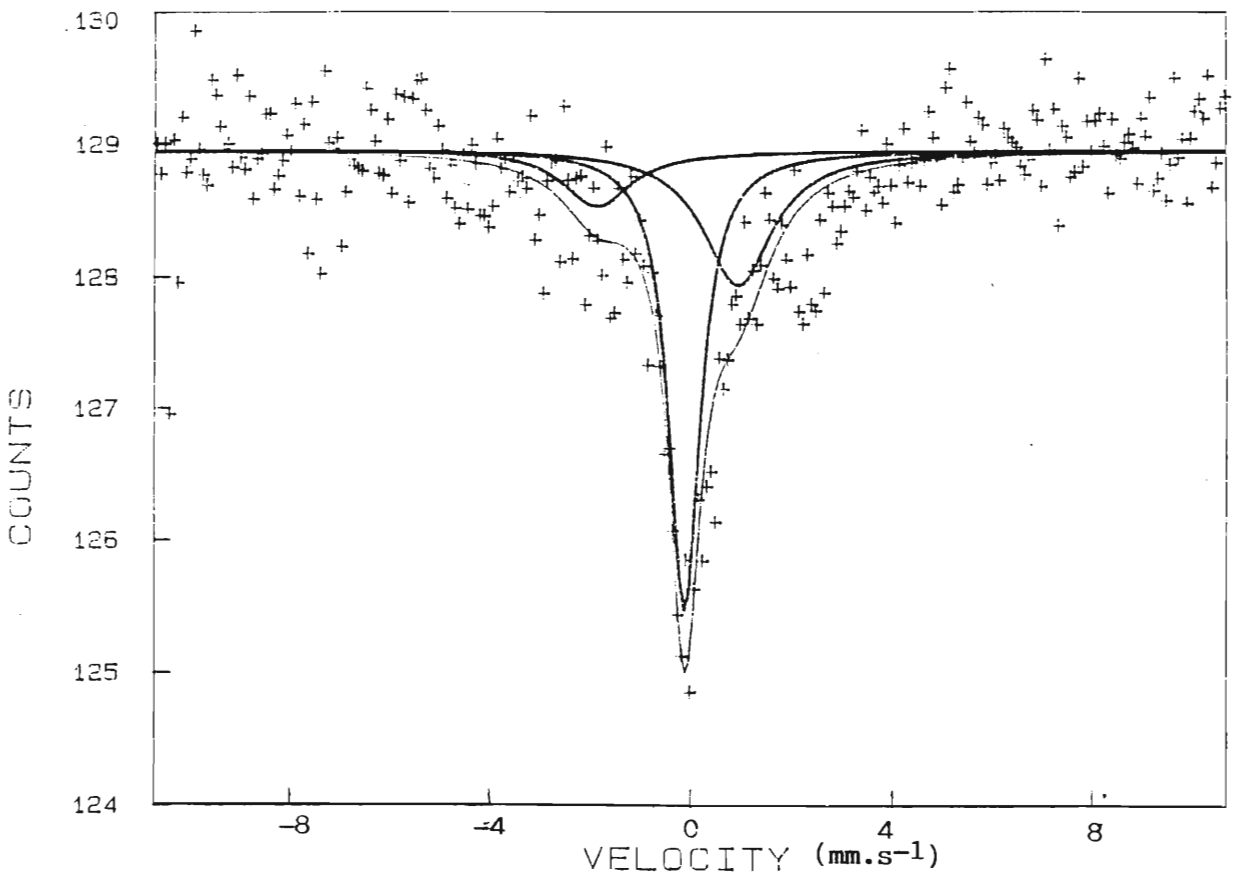

FIGURE 4 (b): ^{57}Fe Mössbauer spectrum for synthetic MDAS diamonds of grain size 105-88 μm (mesh 100/140).

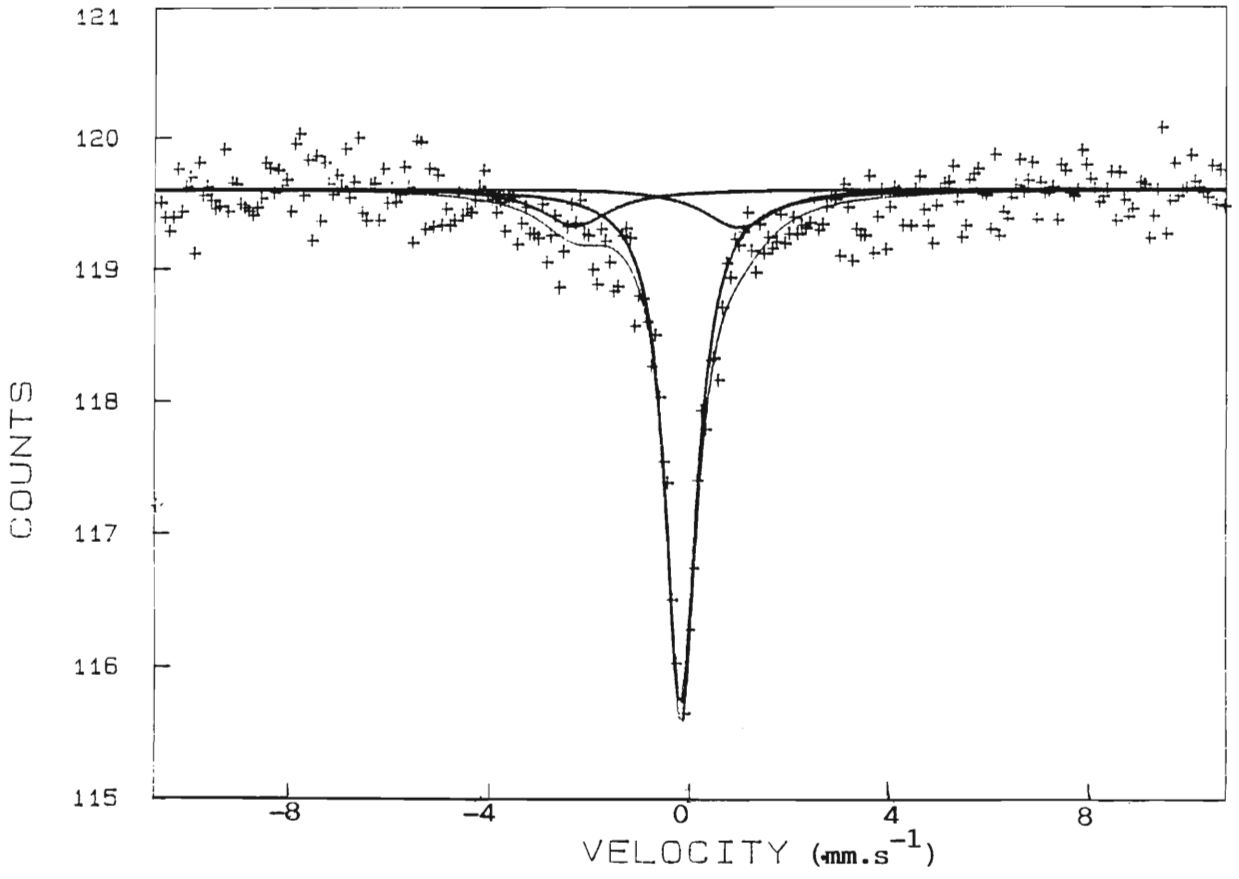

FIGURE 4 (c): ^{57}Fe Mössbauer spectrum for synthetic MDAS diamonds of grain size 75–63 μm (mesh 200).

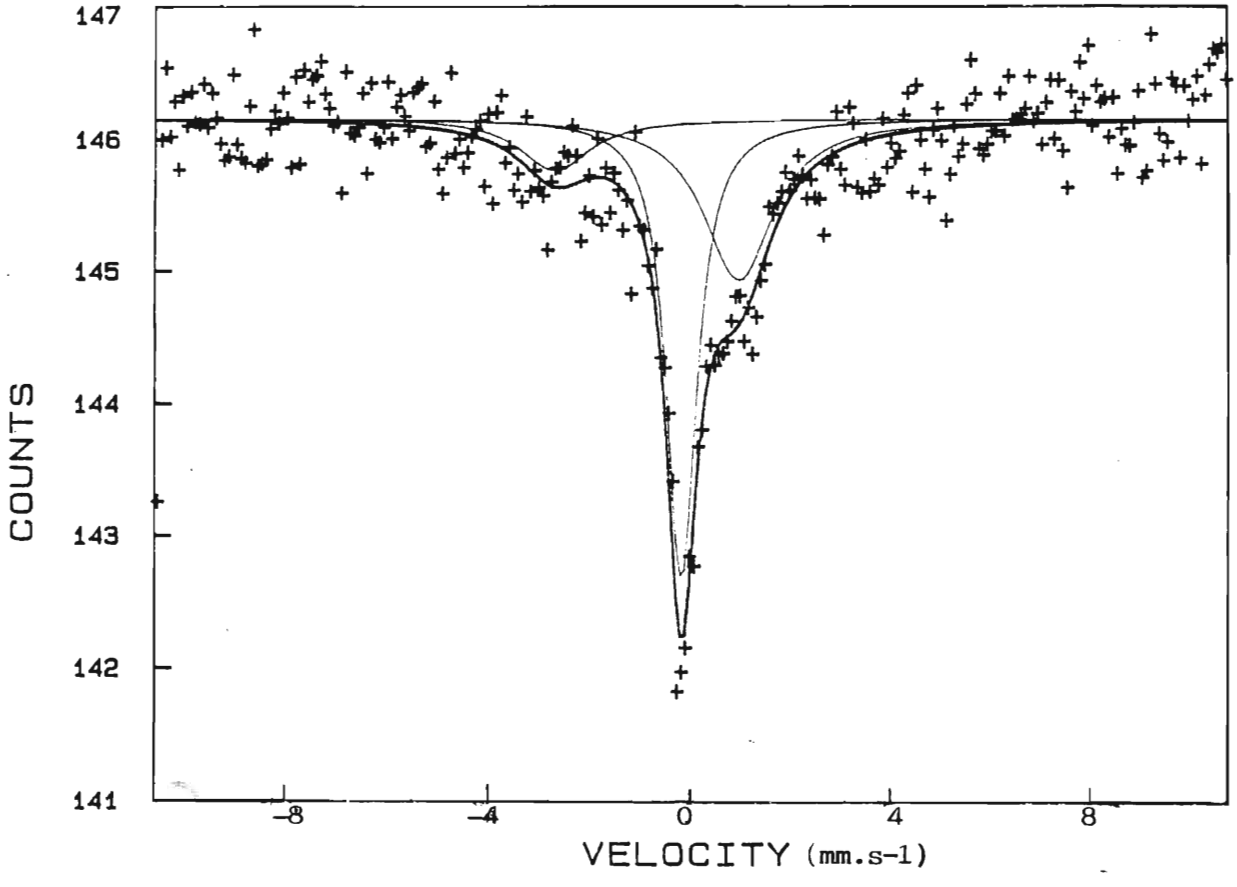

FIGURE 4 (d): ^{57}Fe Mössbauer spectrum for synthetic MDAS diamonds of grain size 50-45 μm (mesh 300).

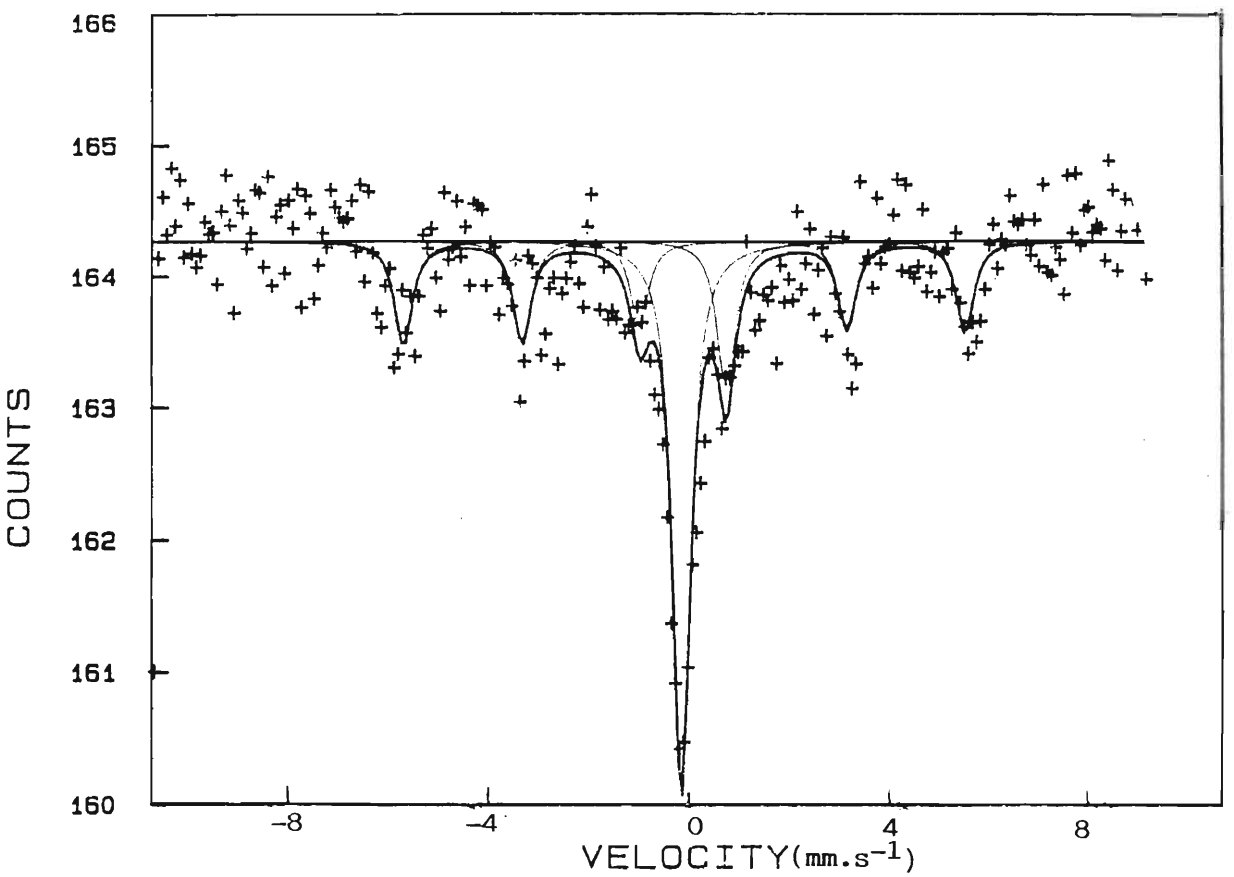

FIGURE 4 (e): ^{57}Fe Mössbauer spectrum for synthetic MDAS diamonds of grain size 38-25 µm (mesh 400/500).

4.2 DATA ANALYSIS

4.2.1 CORRELATED LORENTZIAN LINESHAPE THEORY

The Mössbauer data were analysed with the aid of the analysis code MOSFUN [Mü80]. In this code a Mössbauer spectrum is treated as a composition of m Lorentzian-shaped absorption lines of intensity W_i, position E_i and full widths at half-maximum (FWHM) τ_i. The theoretical value of the intensity F at the velocity V is then given by [Mü80]

$$F(V) = g \{ N_\infty - \sum_{i=1}^{m_i} [W_i/(1 + a_i^2)] \}, \quad a_i = (V - E_i)/\tau_i \qquad (4.1)$$

where g is a geometrical correction factor at velocity V, and N_∞ is the base line.

W_i, E_i and τ_i represent the parameters of line i.

If these lines are correlated because of quadrupole or magnetic interactions it follows that the line parameters are not independent.

The Mosfun code correlates the line parameters linearly and the fit parameters are the independent variables e.g.,

$$W_i = \sum_{k=1}^{m_i} C_{i,k} P_k$$

where m_i = number of intensity parameters P_k.

The matrix C (dimension $m_i \times m_i$) contains the coefficients of the system of linear equations. For positions and half widths analogous relations are formulated, the corresponding coefficient matrices have the dimension $m_i \times m_p$ (M_p = number of position parameters) and $m_i \times m_g$ (M_g = number of width parameters). In this program the three matrices are put together to form a matrix $m_i \times (m_i + m_p + m_g)$. Only line parameters of the same kind can be correlated e.g. position with position.

4.2.2 FOLDING

In using the MOSFUN programme, the experimental data is brought into the required form. The spectrum is then plotted and inspected for dropped channels. Since the second half of a full absorption spectrum is a mirror image of the first half due to the source moving through an interval V_{min}-V_{max}-V_{min}, the spectrum is folded.
A comparison of the folded and unfolded spectra was made so as to ensure that no broadening of lines were introduced.

4.2.3 FITTING A MÖSSBAUER SPECTRUM

The peak parameters determined from the plot is used as starting values in MOSFUN to fit the data, using equation (4.1). With these starting values a theoretical spectrum is plotted and X^2 (the goodness of fit parameter) is calculated.

During a calculation the program permits the application of various constraints. The base, geometry and folding point parameters are usually fixed while the other parameters i.e., position, intensity and half-widths may be released stepwise. This is done in order to avoid divergence and save computing time. Iterations can then proceed by choosing either the Newton or Gradient method. The former is normally attempted first as convergence is reached quickly, after which the Gradient method may be chosen [Mü80]. The fitted Mössbauer spectra is then analysed in terms of hyperfine interactions.

4.3 RESULTS

The values of the various parameters extracted from the spectra are tabulated in Table 4.1.

Table 4.1 : ^{57}Fe Mössbauer parameters for synthetic MDAS diamonds of different grain sizes.

Mesh	Grain Size (μm)	Isomer Shift δ ($mm.s^{-1}$)		Magnetic Hyperfine Field (T)	Electric Field Gradient ($V.cm^{-2}$)
		Single line	doublet		
60/80	250-180	-0.46(1)	-	-32.4(4)	
100/140	105-88	-0.45(3)	-0.80(7)	-	$1.4(4) \times 10^{18}$
200/230	75-63	-0.51(7)	-1.00(9)	-	$1.6(4) \times 10^{18}$
300/325	50-45	-0.49(6)	-1.26(9)	-	$1.8(7) \times 10^{18}$
400/500	38-25	-0.46(3)	-	-27.4(7)	

4.4 SYNTHESIS OF RESULTS

4.4.1 MAGNETIC HYPERFINE FIELDS

The positions of the resonance lines in a Mössbauer spectrum of an absorber in which the energy levels are magnetically split and recorded with an unsplit gamma source are given by [Ko84]

$$v(m_e,m_g) = \delta + \mu_g H(c/E_o)\{m_g/j_g - m_e/j_e\ (\mu_e/u_g)\} \qquad (4.2)$$

The magnetic moment ratio is given by

$$\mu_e/\mu_g = -3g_1/g_o \qquad (4.3)$$

where g_1 is the splitting of the excited state and g_o is the splitting in the ground state.

Knowing μ_g and the separation of the spectral lines, μ_e can be determined from [Go68]

$$\mu_e = -3\mu_g \frac{V_{3/2 \rightarrow 1/2} - V_{1/2 \rightarrow 1/2}}{V_{1/2 \rightarrow 1/2} - V_{1/2 \rightarrow -1/2}} \qquad (4.4)$$

The value of μ_g (^{57}Fe) = +0.0903 ± 0.0007 μ_N was obtained by Ludwig and Woodbury [Go68].

Substituting the known line positions, the isomer shift δ and the ratio of the magnetic dipole moments of the nuclear excited and ground states, μ_e/μ_g, in equation (4.2), the magnetic field, H, can be evaluated.

The magnetic moment ratio, calculated using equation (4.3) was -1.69(4) for the iron foil, -1.74(4) for the 180-250 μm diamond sample and -2.23(5) for the 38-25 μm, the smallest diamond grain size.

Using μ_g, the values of μ_e = -0.153 μ_N for the iron foil, -0.157(5) μ_N for the 180-250 μm diamond sample and -0.201(8) for the 38-25 μm diamond sample, respectively, were obtained.

A value of B_{hf}= -33.3(2) T was calculated for the magnetic hyperfine field of the iron foil at room temperature. The negative sign of the hyperfine field indicates that the field aligns antiparallel to the magnetization as well the dominance of core-polarization terms.

An effective magnetic hyperfine field of B_{hf} = -32.4(4) T was obtained for the 250-180 μm diamond grains. This value of the magnetic field and the magnetically split spectra obtained (Figure 4 (a)), indicate that the Fe inclusion in these grains aggregate as undisturbed body centred cubic α-Fe.

For diamond grains (38-25 μm), the magnetic field decreased and a value of B_{hf} = -27.4(7) T was obtained.

4.4.2 ELECTRIC FIELD GRADIENTS (EFG)

The excited state of the ^{57}Fe nucleus has a spin I=3/2 and in the presence of a non-zero electric field gradient this splits into two substates, with m = ± 1/2 and ± 3/2. This leads to a two line spectrum with the two lines separated by the quadrupole splitting. The two levels are separated in energy by

$$E_Q = e^2qQ/2 \; (\; 1 + \eta^2/3)^{1/2} \qquad (4.5)$$

where : Q is the quadrupole moment of the nucleus

e is the charge of the electron

η is the asymmetry parameter.

It is conventional to specify the EFG in terms of its z-component defined by

$$V_{zz} = eq \qquad (4.6)$$

and an asymmetry parameter η where,

$$\eta = \frac{V_{yy} - V_{xx}}{V_{zz}} \qquad \text{with } |V_{zz}| > |V_{yy}| \geq |V_{xx}|.$$

Equation (4.6) can be substituted in equation (4.5) to obtain

$$Q.S = eV_{zz}Q/2 \qquad (4.7)$$

The quadrupole splitting can be obtained from the Mössbauer spectrum and using equation (4.7), V_{zz} (EFG) can be calculated.

Analysis of the splitting for diamond grain sizes 105–45 μm gives an estimated value of the efg at the ^{57}Fe probe nucleus in the range of V_{zz} = 1.5(3) x 10^{18} V.cm^{-2}. This is in reasonabl agreement with the value 1.2(2) x 10^{18} V.cm^{-2}, determined for implanted ^{57}Fe in natural diamond [Sa83].

5. DISCUSSION

5.1 FERROMAGNETIC TO SUPERPARAMAGNETIC TRANSITION

In order to understand the dramatic change in the Mössbauer spectra in going from grain sizes 250 to 45 μm, we compare our results with other relevant measurements.

5.1.1 Mössbauer study of Fe under high pressure

In the first experiments Pound et al. [Po61] investigated changes in isomer shift for an iron absorber subjected to high pressures up to 0.3 GPa. Their results showed that isomer shift of iron changed linearly with pressure. They attributed the change to a phase change from body centred cubic (bcc) phase to hexagonal close packing (hcp) phase as the volume decreased.

X-ray diffraction measurements at high pressure also confirmed that the high pressure phase of iron is hcp [Ja62]. Similar observations were made by Nicol and Jura [Ni63], who had analysed the Mössbauer spectrum of iron up to 14 GPa using Bridgman anvils. Their results indicated that in the α-Fe phase the isomer shift was $\delta = 0.127$ mm.s^{-1}. and also that their source was partially transformed to the hcp phase. The isomer shift in the hcp phase was 4 x larger than in the α-phase. They concluded that this may also arise as a result of the transition from a ferromagnetic phase to a paramagnetic phase.

Mössbauer spectrum of ^{57}Fe in iron has also been measured up to pressures of 24 GPa [Pi64]. Below 3 GPa, the spectrum consisted of the normal 6 lines characteristic of ferromagnetic bcc iron. The internal magnetic field B_{eff} decreased with volume. The isomer shift(s) shifted with pressure indicating an increase in s-electron density at the nucleus.

Above 13 GPa, a 7th line appeared near the centre of the spectrum due to the transformation of part of the iron source to hcp high pressure phase.

With increasing pressure (up to 21.6 GPa) the line became more intense and the magnetically split spectrum disappeared although the transformation was sluggish. A strong central paramagnetic component was formed. From the absence of splitting, Pipkorn et al.[Pi64], concluded that the internal field in the hexagonal phase was 0 ± 0.3 T. There was a small broadening due to electric quadrupole interaction in the hexagonal lattice. The isomer shift δ of the hexagonal relative to cubic phase was $-0.7\ mm.s^{-1}$. This indicated that the s-electron density was greater in the hexagonal phase.

For metallic iron, it was also observed that the internal magnetic field and isomer shift both decreased linearly with increasing pressure [Ok69].

The advent of the diamond anvil cell (DAC) for measuring in situ pressures have allowed measurements to be made in the 100 GPa region. ME-DAC data on Fe metal to 45 GPa [Na86], clearly showed phase changes at room temperature.

Taylor et al.[Ta90/91] also attributed the change in their high pressure measurements to a phase change of Fe from bcc α-Fe to hcp ε-Fe (see Figure 5.1). In Mössbauer Spectroscopy-diamond anvil cell (MS-DAC) measurements on ^{57}Fe they found that at room temperature and at a pressure of about 11 GPa bcc or α-Fe begins to transform into hcp phase called ε-Fe that is non-magnetic. They observed a sluggish change in the magnetically split spectra as the pressure increased from 0.55 GPa to 23.3 GPa. At 23.3 GPa, a central unsplit (nonmagnetic) line appeared arising from the appearance of ε-Fe. When the pressure was reduced to 9.5 GPa, about half of the ε-Fe transformed to α-Fe. A small remnant of ε-Fe was still present at 7.7 GPa.

In the present study, the changes in the Mössbauer spectra for the diamond grains mimics the DAC measurements of Taylor et al. For the largest grain size (Figure 4(a)), the value of the effective magnetic hyperfine field at the Fe probe of B_{hf} = -32.4(4) T as well as the sextet structure confirms that the Fe inclusions aggregate as bcc α-Fe. The small central peak can then be attributed to hcp ε-Fe [Pi64] phase and is possibly due to the Fe atoms in diamond being subjected to high pressures.

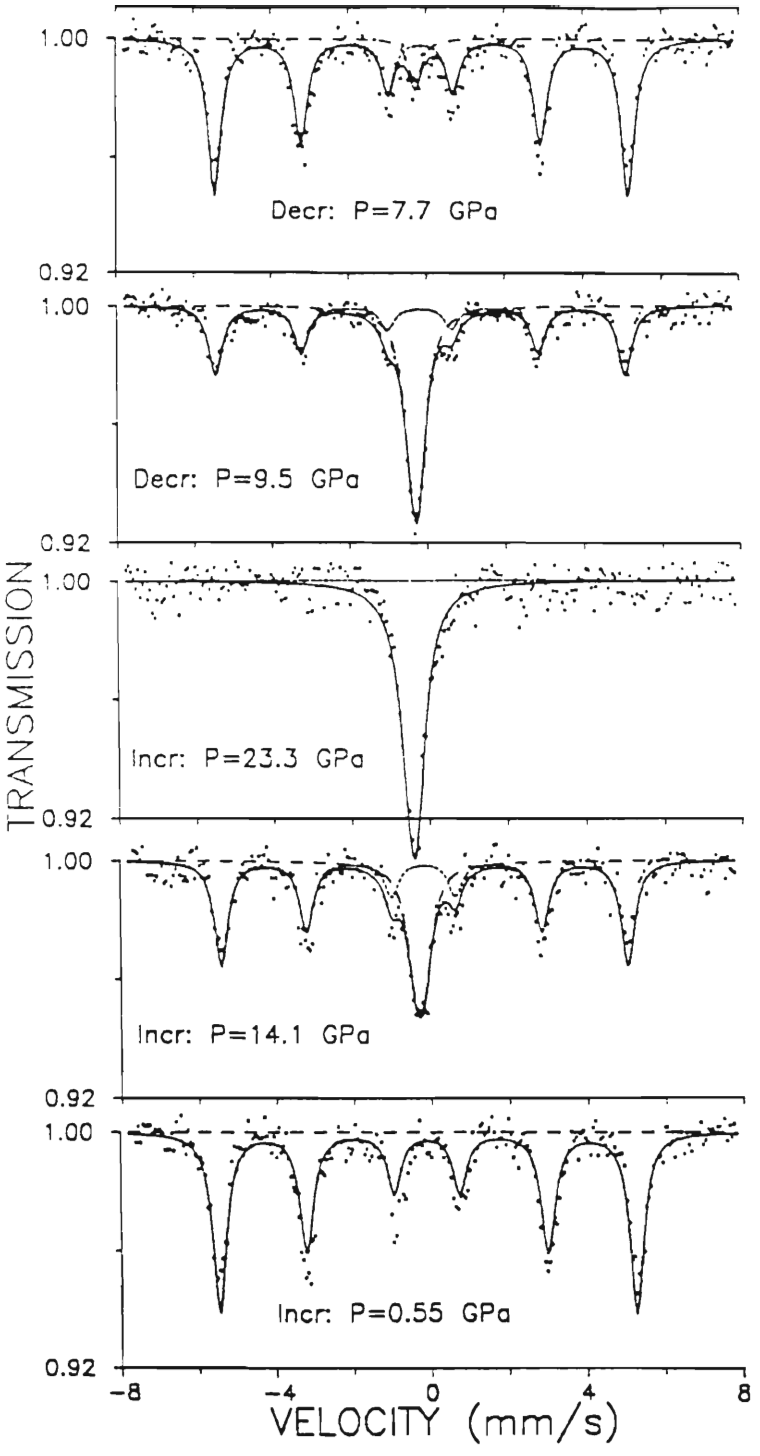

FIGURE 5.1 : Mössbauer spectra of an enriched Fe absorber in a diamond anvil cell (DAC) at increasing and decreasing pressures [Ta91].

A drastic decrease in the magnetic hyperfine field and a rapid increase in the intensity of the central single line was observed in going from 250 to 45 μm diamond grain sizes (refer to Figure 4 (a)-(d)). From the studies by Pipkorn et al. [Pi64] and Taylor et al. [Ta91], the changes in the spectra can be explained as being due to the transformation of bcc α-Fe under high pressures to hcp ε-Fe.

As the grain sizes decrease from 105 to 45 μm, the isomer shift (refer to Table 4.1) of the single line is more negative and hence implies that the total s-electron density $|\psi(0)|^2$ at the Fe nucleus increases. This effect can be associated with the small volume available for the Fe sites in the diamond matrix [Sa90], leading to a large compression of the s-electron shells of the Fe atom.

From the isomer shift data (Table 4.1), it can be concluded that as the grain sizes decreases, the Fe atoms in these diamond samples are exposed to increasingly high pressures. The large values of internal pressure of Fe in diamond must be due to very strong bonds between carbon atoms [Sa81] and also due to a large difference in the atomic volumes of the host and the inclusion (atomic radii of carbon and iron atoms are 0.77 Å and 1.26 Å, respectively).

5.1.2 Superparamagnetism

An alternative interpretation is that the changes observed is due to a phase transition of the Fe from ferromagnetic to superparamagnetic.

In ferromagnetic materials eg. Fe, there is a strong tendency for the material to break up into magnetic domains (regions in which the dipoles are aligned), each with a different direction of magnetization so that the macroscopic effect is to give zero magnetization. The boundaries separating magnetic domains are called domain or Block walls. Two ferromagnetic phenomena are based on particle size. In the first, domain walls are lost below a critical size and particles become single domains. For Fe, single domain particle size occurs for diameter $\approx$ 210 Å [Go91]. In the second, exchange forces are lost below a second, smaller critical size and materials become paramagnetic [Bu86].

Karfunkel et al.[Ka85] have suggested that the collapse of the magnetic hyperfine structure from the larger to the finer grain may be a case of superparamagnetism due to the breakdown in alignment of the fine single domain particles.

Superparamagnetism occurs in small particles of magnetically ordered materials [Do90]. The magnetic energy of a particle is proportional to its volume and for small particles the magnetic energy is comparable to the thermal energy. Under

these circumstances the magnetisation vector is not fixed along one of the easy directions as in large crystals, but fluctuates. In this case, a particle changes back and forth between domain and no-domain structures. In the no-domain state below the second critical size, ferromagnetic materials are said to experience superparamagnetism.

The essential condition for observation of a magnetically split pattern is that τ (relaxation time of domain alignment) must be greater than the observation time τ_o i.e., the lifetime of the excited state of ^{57}Fe nucleus (τ_o = 144 ns for ^{57}Fe). Thus, for observing a magnetically split pattern

$$\tau \gg 144 \times 10^{-9} \text{ s.}$$

For $\tau \ll \tau_o$, no magnetic effect is observed and a paramagnetic spectrum is formed.

Studies of particles in the superparamagnetic state allow for the determination of the particle size. From the relationship [Mϕ90],

$$\tau = \tau_o \exp\{-KV/kT\}$$

where k is the Boltzmann constant, T is the temperature, K is the effective anisotropy energy and V the volume of the particle, Karfunkel et al. estimated the critical iron particle size ≈ 100 Å for paramagnetism to set in [Ka85].

However, Gong et al.[Go91], using the magnetic domain theory calculated the critical radius R_c of the single domain size of Fe from $Rc = 9/2\ \pi\sqrt{AK/M^2_s}$, where M_s, A and K express magnetic saturation, exchange constant and anisotropy constant respectively. The R_c (calculated) = 98 Å compared favourably with R_c (experiment) = 105 Å. It was shown that with the decrease of the diameter of the particle size 210 Å, the magnetic properties entered the superparamagnetic region.

Mössbauer spectra of ultrafine particles of amorphous $Fe_{1-x}C_x$ obtained at temperatures between 12 K and 120 K, showed that the spectrum (at 12 K) consisted of a magnetically split spectrum and a quadrupole doublet. The magnetically split component was due to the $Fe_{1-x}C_x$ particles. At higher temperatures the six-line component decreased and a broad singlet component appeared. This indicated that the $Fe_{1-x}C_x$ were superparamagnetic. Superparamagnetism has also been recorded with ^{57}Fe in metal alloys, where it is attributed to a reduction in particle size or to magnetic dilution [Gr71].

The diamond samples used in the present study have grain sizes several orders of magnitude larger than the critical size for paramagnetism to set in.. The grain sizes 105-25 μm where a strong paramagnetic component appeared in the spectra suggest that the Fe inclusions less than 210 Å in size and that the changes in the spectra may be due to the onset of superparamagnetism.

5.1.3 Reappearance of ferromagnetically split spectrum for grain sizes 38-25 μm.

At first sight one may conclude that the synthesis of larger grain size is accompanied by the growth of larger sized Fe inclusions by diffusion or aggregation [Ka85]. However, the reappearance of the ferromagnetic split Mössbauer lines for the smallest diamond grain size 38-25 μm (Figure 4 (e)), argues against this. Similar behaviour has been previously reported for synthetic CDA diamonds [Ka85]. We now examine possible alternatives which may explain the observed spectra.

A possible interpretation of the spectra may suggest the presence of two phases, a phase with magnetic order and a phase without magnetic order. As discussed in Section 5.1, the central single line (phase without magnetic order) is attributed to hcp ε-Fe atoms under high pressure [Ta90] or to small dimensional Fe inclusions exhibiting superparamagnetic behaviour [Ka85, Go91].

To account for the magnetically split components in the spectra, Fe clustering has already been ruled out as a possible explanation.

In the MS-DAC experiment [Ta91], about half of the ε-Fe transformed to α-Fe upon reducing the pressure to 9.5 GPa and the intensity of the central non-magnetic line correspondingly decreased (refer to Figure 5.1). However this was not

the case in this study for diamond grain sizes 105–38 μm where the intensity of the central line remained fairly constant. This suggests that no transformation of hcp ε-Fe to the bcc α-Fe phase has occurred and that the appearance of the magnetic spectra must be due to some other effect.

Among the phenomena encountered in disordered magnetic materials, re-entrant magnetic behaviour has been observed in $Au_{1-x}Fe_x$ [Me90]. Meyer interpreted this at low temperatures as due to giant moments of weakly interacting superparamagnetic clusters and not to the ordering of individual moments. This was proposed on the basis of a theory by Mϕrup for weakly interacting particles. Beck [Be85] proposed a similar interpretation of the magnetic structure but in terms of fluctuating superparamagnetic clusters. He obtained an increasing size of the clusters when lowering the temperature together with a gradual decreasing of intercluster coupling exchange constant.

From the above, we suggest that the reappearance of the magnetically ordered phase may possibly be due to interacting supermagnetic clusters of Fe [Be85, Me90].

An alternative explanation of the spectra for the smallest diamond grain size arises from iron carbide studies.

In the iron-graphite system at high pressure and at high temperature, it is known that Fe_3C(cementite) is metastable to α-Fe and graphite [Ts84]. From investigations of alloys of Fe

with carbon [Pu89] at high pressures and temperatures, the conclusion drawn is that in the Fe-C system the existence of a carbide is a necessary condition for the formation of diamond.

In the initial stage of diamond synthesis in Fe-Ni alloy plates combined with graphite [Pe90], a number of small particles besides diamond are formed, which are considered as a compound of iron and carbon i.e., a carbide.

The microstructure of the metallic inclusions in synthetic diamond crystals grown in Fe-C systems at a pressure of $\approx$ 5.5 GPa and at a temperature of $\approx$ 1800 K were studied by Pavel et al.[Pa90]. From high-pressure phase diagrams for Fe-C, it was observed that Fe_3C was the only stable carbide at 5.5 GPa. Scanning electron microscopy(SEM) investigations identified the metallic inclusions as ledeburite eutectic (Fe_3C + fcc Fe).

Further investigations showed that with the increasing size of the metallic inclusions in diamond crystals, a decreasing carbide contribution in favour of ledeburite eutectic appeared. It is therefore expected that with decreasing size of the metallic inclusions, the carbide contribution should increase.

Nuclear gamma resonance(NGR) spectra analysis of Fe-Ni metallic inclusions in synthetic diamonds [Ba90] divided the samples into two groups. The first group contained inclusions with and

without magnetic order. The magnetically ordered phases (10^4 Å in size) is assigned to Fe-Ni alloy clusters. The phase without magnetic order is assigned to Fe, Ni and FeNi small dimensional inclusions(≈100 Å) and showing superparamagnetic properties. NGR spectra show evidence of $(FeNi)_3$ carbide phase, in agreement with X-ray diffraction measurements. The second group contained inclusions without magnetic order, due to superparamagnetic domains and to large size (10^4 Å) fcc (FeNi) alloy clusters.

Thus, from iron carbide studies, the reappearance of the Mössbauer spectra for grain sizes 38-25 μm can also be attributed to the presence of a carbide, presumably Fe_3C.

In summary, for diamond grain sizes of 38-25 μm, it is suggested that there are two phases present, a magnetically ordered phase which may be due to weakly interacting superparamagnetic clusters of Fe or to a carbide, presumably Fe_3C which is also ferromagnetic [Gr71] at room temperature and a phase without magnetic order attributed to hcp ε-Fe atoms under high pressure [Ta90] or to small dimensional Fe inclusions exhibiting superparamagnetic behaviour [Ka85, Go91].

5.2 THE ELECTRIC FIELD GRADIENT AT Fe SITES IN DIAMOND.

For diamond grain sizes 105-45 μm (Figure 4 (b)-(d)), a central single line and an asymmetric quadrupole-split doublet was obtained. The quadrupole splitting also increased as the grain size decreased.

In studies of ^{57}Fe implanted into diamond crystals, Mössbauer spectra also showed a quadrupole-split doublet [Sa90]. The quadrupole-split doublet was ascribed to the impurity atoms occupying low symmetry (LS) sites. A large value of the EFG i.e., $V_{zz} = 1.2 \times 10^{18}$ V.cm^{-2} at 4 K was obtained for these sites. There was a very small temperature dependence of the quadrupole splitting between 4 and 300 K. This indicated that the distribution of electrons and ions producing the EFG at the Fe nuclei at LS sites remained almost unchanged.

Mössbauer spectra of amorphous $Fe_{1-x}C_x$ at low temperatures also revealed a quadrupole doublet.This was due to Fe(II) in the high spin state [Mϕ89].

In this study, the observed splitting for grain size 105-45 μm yielded a large value of the electric field gradient at the Fe nucleus of $V_{zz} = 1.5(3) \times 10^{18}$ V.cm^{-2}. This is in reasonable agreement with the value determined for implanted ^{57}Fe in natural diamond [Sa83]. Sawicka et al. [Sa90] suggested that the EFG originates from low-symmetry (non-

cubic) distribution of the nearest carbon atoms. Thus the LS sites may be associated with the defective regions in the diamond lattice [Sa81]. On the other hand, Bharuth-Ram et al. [Bh91a], suggested that the quadrupole doublet may be due to a small fraction of the Fe forming Fe-C bonds at substitutional sites in the diamond lattice.

In studies of size changes of lattice parameters in ultradisperse diamond powder (4.6 nm), it was estabilished experimentally and theoretically that when decreasing the sizes of the crystals, the lattice parameters increased [Ga90]. This was explained by the size change of intracrystalline pressure stipulated by the interaction of excess negative charges arranged on the bond lines C-C, and the positive cores of the atom of the covalent crystal. As the particle sizes decreases, the number of interacting atoms decreases and, as a result, the contribution of attractive forces due to intracrystalline pressure decreases, and the lattice expands. This expansion is not due to the higher content of impurities in the structure of small particles but due to the decrease of sizes of particles.

Mössbauer data for Fe and Co implants in diamond, graphite and other matrices of the carbon family, revealed that the EFG at LS sites increases with an increase in the interatomic distance of the host matrix. This was explained as due to the relaxation of the volume compression of Fe atoms in

defective regions [Sa81].

In this study, the quadrupole splitting increased significantly as the grain size decreased as shown in Table 4.1. This may be due to a greater fraction of Fe forming Fe-C bonds or to a decrease in the compression of Fe atoms at LS sites with a corresponding decrease in the particle size .

5.3 THE NATURE OF IRON SITES IN DIAMOND.

Sawicka et al.[Sa90] indicated that Fe ions occupy two sites in diamond, a high symmetry (HS) and a low symmetry site (LS). About 20 % of the implanted ions ended up in HS sites, with the remaining 80 % of ions in LS sites. The HS sites are characterised by very high Debye temperatures $\Theta_D \approx 1300$ K and by high s-electron densities. The single line component of the Mössbauer spectra confirms that Fe atoms are exposed to high pressure [Ta91] and that they occupy HS sites (presumably substitutional or tetrahedral interstitial). The quadrupole doublet is attributed to Fe atoms resting at LS sites in the diamond matrix. The LS sites are characterized by a large EFG and a Debye temperature of 550 ± 50 K. It was also shown that the two types of sites exhibit very different temperature dependences with the quadrupole splitting changing very little in the temperature range of 4-300 K.

Lowther [Sa90] speculated about the positions of iron atoms in diamond and their possible electronic configurations based on molecular cluster orbital calculations. One result suggest that the occupancy of the 3d shell of Fe atom on the substitutional site is decreased by the gain of the 4s shell which enters into chemical bonding with the surroundings.

In diamond grain sizes 105-45 μm, a central single and a quadrupole split spectra was obtained. This indicates that the Fe atoms occupy two distinct sites in the diamond lattice. The single spectrum suggest that Fe atoms (hcp ε-Fe) are under high pressure and occupy non-damaged sites in the lattice (HS sites), presumably, substitutional sites.

The large value of the EFG obtained from the quadrupole doublet suggests that a large fraction of Fe atoms occupy sites in non-cubic surroundings. From Lowther's [Sa90] and Bharuth-Ram's speculations [Bh91a], we suggest that the Fe atoms in these regions enters into chemical bonding with the carbon lattice and this may result in the formation of Fe-C bonds. Although interstitial sites have been suggested for Fe atoms occupying LS sites [Sa90], we are not able to propose, at present, the position of Fe at low-symmetry sites.

5.4 PROBE DEPENDENCE OF THE ELECTRIC FIELD GRADIENT

Finally in Table 5.1 we compare the value of the electric field gradients in diamond determined with different nuclear probes. The Table shows our results, together with that determined for ^{19}F, ^{111}In and ^{181}Hf probes.

TABLE 5.1 : Comparison of efg (V_{zz}) values for different probe atoms in diamonds.

Probe atom	Atomic number Z	Probe radius R (fm)	V_{zz} (x 10^{18} V.cm.$^{-2}$)	Reference
^{19}F	9	3.2	3.4(2)	[S-H92]
^{57}Fe	26	4.62	1.5(3)	this work
^{57}Co	27	4.62	1.2(2)	[Sa83]
^{111}In	49	5.77	0.64(1)	[Ap81]
^{181}Hf	72	6.79	0.50(5)	[Ra83]

The electric field gradient, V_{zz}, in diamond sensed by the different probes are plotted in Figures 5.1 and 5.2 as functions of the atomic number (Z) and the radius R (= $r_oA^{1/3}$) of the probe nucleus.

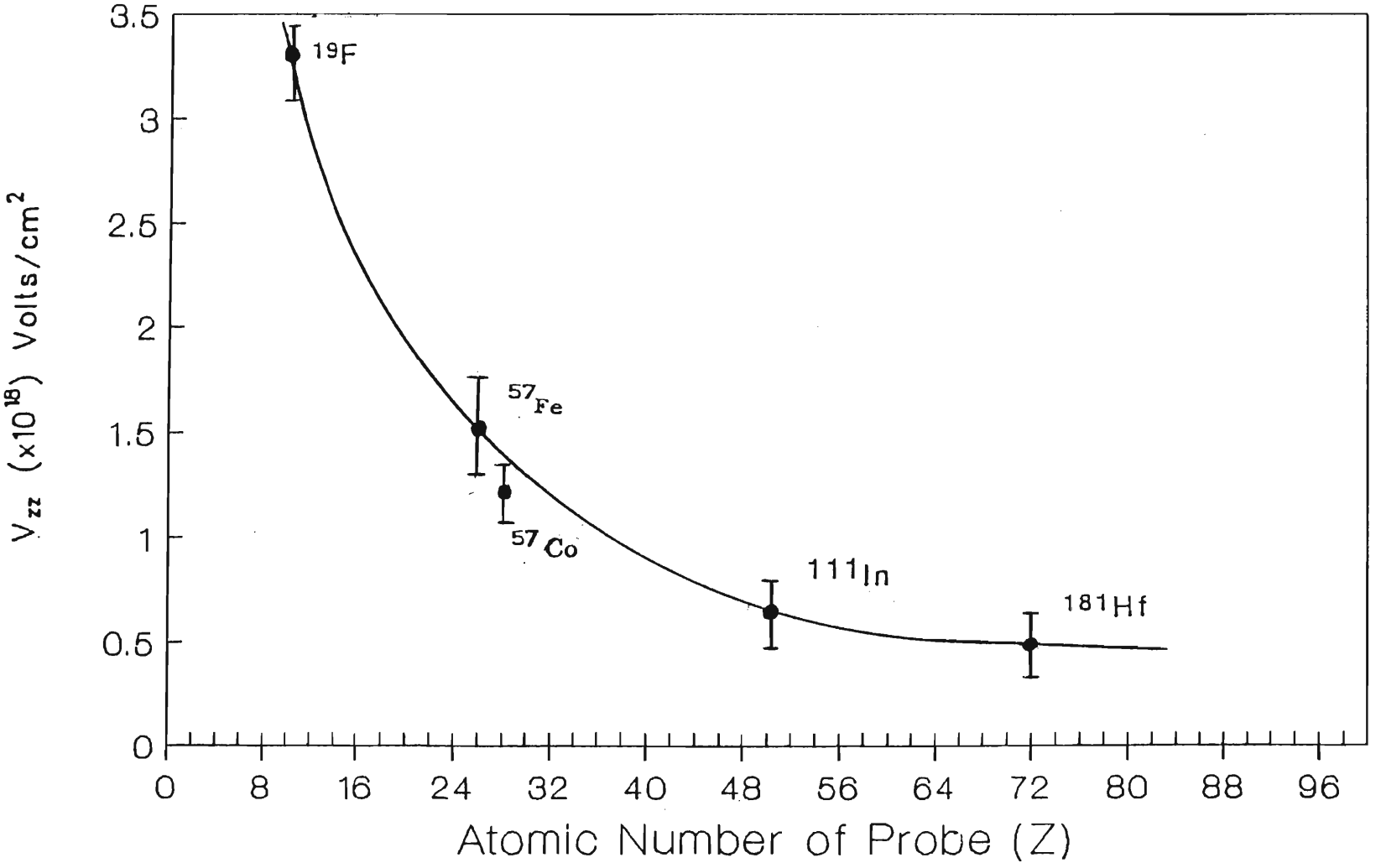

FIGURE 5.2: The electric field gradient (V_{zz}) dependence in diamond on the atomic number (Z) of the probe nucleus

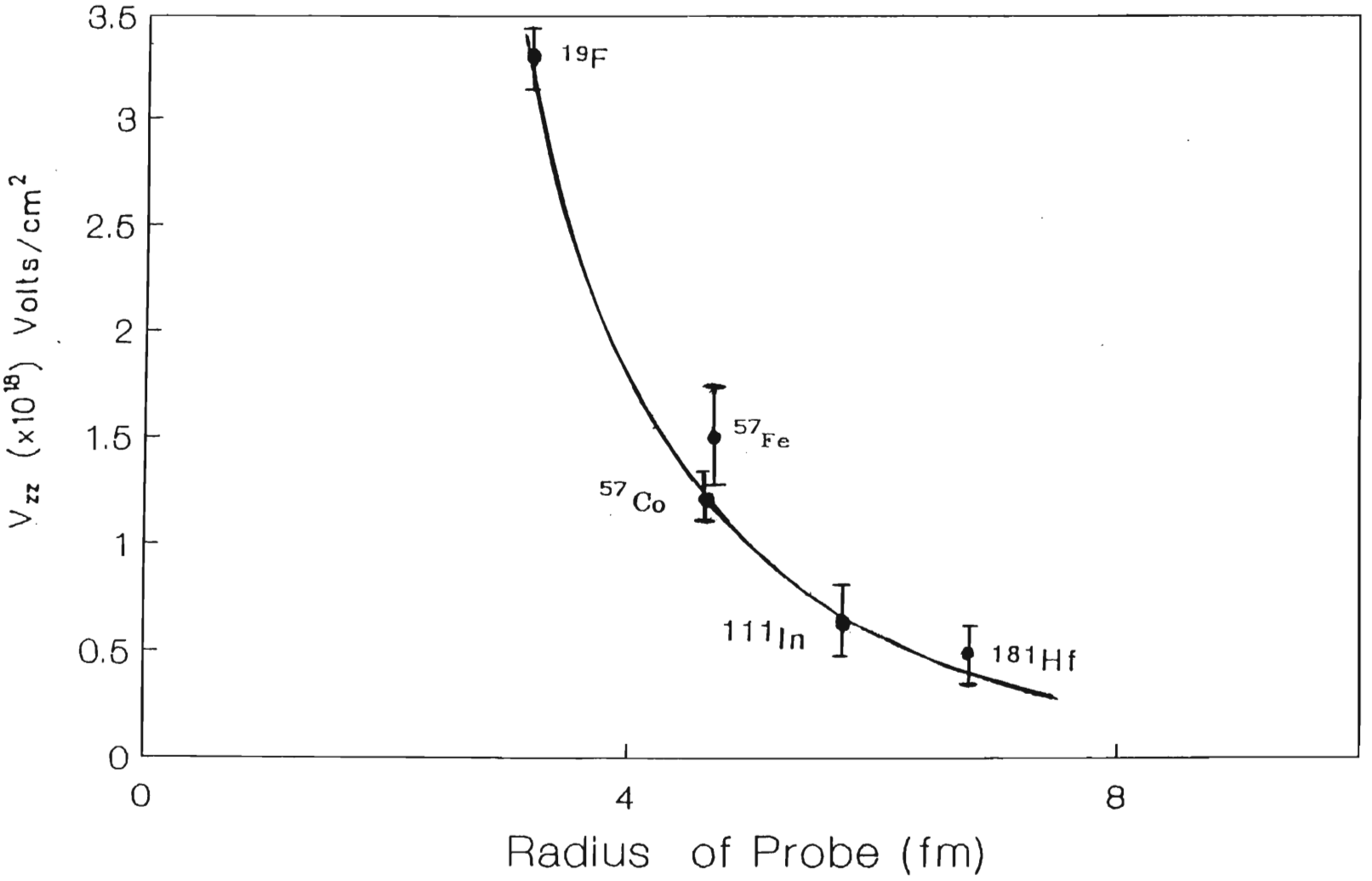

FIGURE 5.3: The electric field gradient (V_{zz}) dependence in diamond on the radius R ($=r_o A^{1/3}$) of the probe nucleus.

A display of the electric field gradient determined for ^{57}Fe probe nucleus in the present work is presented in Figure 5.2, together with the values determined with ^{19}F [S-H92], ^{57}Co [Sa83], ^{111}In [Ap81] and ^{181}Hf [Ra83] ions as a function of Z, the atomic number of the probe ion. The results fit in nicely with the systematic trend reported by Connell et al [Co87].

A plot of the EFG's against the radius R (= $r_oA^{1/3}$) of the probe nucleus (Figure 5.3) also presents a systematic trend i.e., the EFG becomes larger at the sites of smaller probes.

6. CONCLUSION

Mössbauer Spectroscopy has been used to study the Fe inclusions in MDAS synthetic diamond grains in the range of 250-25 μm. The Fe inclusions were entrapped in the diamond during the solvent-catalyst process in which the diamond grains were fabricated.

The Mössbauer spectra obtained in the present study for the different grain sizes of diamond are shown in Figure 4 (a) to Figure 4 (e). The samples with the largest grain size of 180-250 μm gave a well defined six component magnetically split spectrum (Figure 4 (a)). This was almost identical to the Zeeman split sextet lines obtained for natural iron (Figure 3.6). A 7th small peak was also observed near the centre of the spectrum.

On going to the smaller diamond grain sizes 105-45 μm (Figure 4 (b)-(d)) the intensity of the magnetically split spectrum becomes greatly reduced and the central single line component increases rapidly in intensity. The spectra are dominated by this central single line (paramagnetic component) with an appearance of a weak asymmetric doublet.

A unique and unexpected observation for the finest grain size 38-25 μm, is the reappearance of the six magnetic hyperfine splitting components together with the strong central single

line paramagnetic component (Figure 4 (e)). The intensity of lines 1,2,5 and 6 of the magnetically split spectra is some what diminished when compared to the 180-250 μm diamond sample.

Karfunkel et al.[Ka85] have suggested that the collapse of the magnetic hyperfine structure from the larger to the finer grain may be a case of superparamagnetism due to the breakdown in alignment of the fine single domain particles. Taylor et al.[Ta90], on the other hand, attributed the change in their high pressure measurements to a phase change of the Fe from bcc α-Fe to hcp ε-Fe.

Pursuing the paramagnetic argument, we note that if the relaxation time τ (of domain alignment) is shorter than the lifetime of the Mössbauer level (τ_o = 144 ns for ^{57}Fe) no magnetic effect will be observed. Studies of particles in the superparamagnetic state allow for the determination of the particle size. From the equation $\tau = \tau_o \exp(-KV/kT)$, where k is the Boltzmann constant, T the temperature, K the effective anisotropy energy and V the volume of the particle, Karfunkel et al. [Ka85] estimated a critical iron particle size $\approx 10^{-2}$ μm (100 Å) for paramagnetism to set in. However, Gong et al. [Go91] using the magnetic domain theory determined the critical diameter to be 210 Å for single domain size for Fe. The diamond samples used in the present study have grain sizes several orders of magnitude larger than the

critical size. The appearance of the paramagnetic component in the spectra therefore suggest that the Fe inclusions should be less than 210 Å in size.

The dramatic changes in the Mössbauer spectra observed in the present study for diamond grain sizes 250-25 μm mimics the Mössbauer Spectroscopy-diamond anvil cell (MS-DAC) measurements of Taylor et al. [Ta91].

For the largest grain size, the value of the effective magnetic hyperfine field of B_{hf} = -32.4(4) T at the Fe probe as well as the sextet structure confirms that the Fe inclusions aggregate as bcc α-Fe. The presence of the 7th small central peak can then be attributed to hcp ε-Fe phase [Pi64] and is possibly due to the Fe atoms in diamond being subjected to high pressures.

A drastic decrease in the magnetic hyperfine field and a rapid increase in the intensity of the central single line was observed in going from 250 to 45 μm diamond grain sizes.

A similar spectra was obtained by Nicol and Jura [Ni63], Pipkorn et al. [Pi64] and Taylor et al. [Ta91], for Fe under high pressure. They concluded that ordinary bcc α-Fe transformed under high pressures to hcp ε-Fe. Hence, a similar conclusion can be drawn to explain the observed changes in the Mössbauer spectra. From the isomer shift data for the

single line (Table 4.1), an increase in the total s-electron density $|\psi(o)|^2$ at the Fe nucleus is associated with the small volume available for the iron sites [Sa90], leading to a large compression of s-electron shells of the Fe atom. The Fe atoms in these diamond samples are thus exposed to increasingly high pressures as the grain size decreases.

For diamond grain sizes 105-45 μm, the central single line and an asymmetric quadrupole-split spectra was similar to that obtained for ^{57}Fe implanted into natural diamond [Sa90]. In accordance with the previous interpretation of the spectra for Co/Fe implanted into diamond [Sa90], the spectra obtained also suggests that the Fe atoms occupy two different sites in the diamond lattice. The single central line is ascribed to Fe atoms occupying high-symmetry (HS) sites [Ar82, Sa90] and the quadrupole doublet to Fe atoms in low-symmetry (LS) sites. The presence of the quadrupole doublet suggests that Fe atoms occupy sites in non-cubic surroundings and are associated with the defective regions [Sa81] in the diamond lattice.

The observed splitting for grain sizes 105-45 μm yielded a large value of the electric field gradient (EFG) at the iron nucleus of V_{zz} = 1.5(3) x 10^{18} V.cm^{-2}. This is in reasonable agreement with the value 1.2(2) x 10^{18} V.cm^{-2}, determined for implanted ^{57}Fe in natural diamond [Sa83].

Sawicka et al. [Sa90] suggested that the EFG originates from low-symmetry (non-cubic) distribution of the nearest carbon atoms. On the other hand, Bharuth-Ram et al. [Bh91a] suggested that the quadrupole doublet may be due a small fraction of Fe forming Fe-C bonds in the diamond lattice. Although interstitial sites have been suggested for Fe atoms occupying LS sites [Sa90], we are not able to propose, at present, the position of Fe at low-symmetry sites.

In this study, the quadrupole splitting at LS sites increased significantly as the grain size decreased as shown in Table 4.1. This may be due to a greater fraction of Fe forming Fe-C bonds or to a decrease in the compression of Fe atoms at LS sites [Sa90] with a corresponding decrease in the particle size.

At first sight one may conclude that the synthesis of larger grain size is accompanied by the growth of larger sized Fe inclusions by diffusion or aggregation [Ka85]. However, the reappearance of the ferromagnetic split Mössbauer lines for the smallest diamond grain size 38-25 μm, argues against this. Similar behaviour has been previously reported for synthetic CDA diamonds [Ka85]. Fe clustering as well as the transformation of hcp ε-Fe to bcc α-Fe has been ruled out to explain the observed spectra.

A possible interpretation of the spectra may suggest the presence of two phases, a phase with magnetic order and a

phase without magnetic order. The central single line (phase without magnetic order) is attributed to hcp ε-Fe atoms under high pressure [Ta90] or to small dimensional Fe inclusions exhibiting superparamagnetic behaviour [Ka85, Go91].

The reappearance of the magnetically split components in the spectra (magnetically ordered phase) may possibly be due to interacting supermagnetic clusters of Fe [Be85, Me90] or to a carbide, presumably Fe_3C which is also ferromagnetic at room temperature. The existence of a carbide is a necessary condition for the formation of diamonds [Pu89] and Fe_3C has been observed in Fe inclusions studies in synthetic diamonds [Pa90].

The presence of ferromagnetic split spectra for the finest grains sizes must still be clearly understood. It will therefore be of interest to investigate further the Mössbauer spectra of smaller sample sizes as well as temperature dependent measurements on synthetic diamonds.

Finally, a display of the electric field gradient determined for ^{57}Fe probe nucleus in the present work is presented in Figure 5.2, together with the values determined with ^{19}F [S-H92], ^{57}Co [Sa83], ^{111}In [Ap81] and ^{181}Hf [Ra83] ions as a function of Z, the atomic number of the probe ion. The results fits in nicely with the systematic trend reported by Connell et al. [Co87].

A plot of the EFG's against the radius R (= $r_o A^{1/3}$) of the probe nucleus (Figure 5.3) also presents a systematic trend i.e., the EFG becomes larger at the sites of smaller probes.

REFERENCES

[An90] Anthony, T.R., Vacuum 41 (1990) 1356.

[Ap81] Appel, H., Raudies, J., Thies, W.G., Hanser, A. and Sellschop, J.P.F., Hyp. Int.10 (1981) 735.

[Ar82] Armon, H. and Sellschop, J.P.F., Proc. Diamond Conference, Oxford, U.K., 1982.

[Ba73] Bancroft, G.M., Mössbauer Spectroscopy (Mcgraw-Hill Publishers, London, 1973).

[Ba90] Barb, D., Lazar, D.P., Rogalski, M., Morariu, M., Pavel, E. and Baluta, G., Rev. Roum. Phys.35 (1990) 247.

[Be85] Beck, P.A., Phys. Rev.B32 (1985) 7255.

[Bh89] Bharuth-Ram, K., Connell, S., Sellschop, J.P.F., Stemmet, M. and Appel, H., Rad. Effects and Defects in Solids 108 (1989) 73.

[Bh91a] Bharuth-Ram, K., Haricharun, H., Govender, N. and Sellschop, J.P.F., Diamond Conference, Oxford, U.K., 1991.

[Bh91b] Bharuth-Ram, K., Haricharun, H., Govender, N. and Sellschop, J.P.F., Int. Conf. on Applications of the Mössbauer Effect, Nanjing, China, 1991.

[Bu86] Burke, H.E., Handbook of Magnetic Phenomena, (Van Nostrand Reinhold Company Inc., New York, 1986) 358.

[Ca62] Cannon, P., J.Am. Chem. Soc.84 (1962) 4253.

[Ch83] Christiansen, J.(ed.) : Topics in Current Physics, (Springer-Verlag, Berlin, 1983).

[Co87] Connell, S., Bharuth-Ram, K., Appel, H., Sellschop, J.P.F. and Stemmet, M.C., Hyp. Int.34 (1987) 185.

[Co90] Connell, S.H., Sellschop, J.P.F., Stemmet, M.C., Appel, H., Bharuth-Ram, K. and Verwoerd, W.S., Hyp. Int.60 (1990) 941.

[De75] Derbyshire, F.J., Presland, A.E.B and Trim, D.L., Carbon 13 (1975) 111.

[Di86] Dickson, P.E. Dominic. and Berry, J. Frank Mössbauer Spectroscopy,(Cambridge University Press, Cambridge, 1986).

[Do90] Dolia, S.N., Krishanmurthy, A., Srivastave, B.K., Indian Pure and App. Phys.28 (1990) 464.

[Fi79] Field, J.E., The Properties of Diamond, (Academic Press, London, 1979).

[Ga90] Gamarnik, M. Ya., Phys.Stat.Sol.161 (1990) 457.

[Gi76] Gibb, T.C., Principles of Mössbauer Spectroscopy, (Chapman and Hall, London, 1976).

[Go68] Goldanskii, V.I., and Herber, R.H., Chemical Applications of Mössbauer Spectroscopy, (Academic Press, New York, 1968

[Go91] Gong, W., Li, H., Zhao, Z. and Chen, J., J. Appl. Phys. 69 (1991) 5119.

[Gr71] Greenwood, N.N and Gibb, T.C., Mössbauer Spectroscopy, (Chapman and Hall, London, 1971).

[Ha60] Hanna, S.S., Heberle, J., Littlejohn, C., Preston, R.S., and Vincent, D.H., Phys. Rev. Lett.4 (1960) 513.

[Ja62] Jamieson, J.C. and Lawson, A.W., J. Appl. Phys. 33 (1962) 776.

[Ka85] Karfunkel, U., Sellschop, J.P.F. and Maguire, H.G., Proc. Diamond Conference, Reading, U.K., 1985.

[Ka90] Kawarada, H., Yokota, Y., Mori, Y., Tomiyama, A., Ma, J.S., Wei, J., Suzuki, J. and Hiraki, A., Vacuum 41 (1990) 885.

[Ko84] Kolk, B., Dynamical Properties of Solids, (Elsevier Science Publishers, B.V., South Africa, 1984).

[Ma78] Massarani, Bo, Bourgoin, J.C. and Chrenko, R.M., Phys. Rev. B17 (1978) 1759.

[Ma86] Maguire, H.G., Morrison, I.E.G., Paige, D.M., Hyp. Int.28 (1986) 607.

[Ma87] Mackenjee, A.T., MSc. Thesis, Univ. Dbn.Westville, 1987.

[Me90] Meyer. C. and Hartmann-Boutron.F., Hyp. Int. 59 (1990) 219.

[Mϕ89] Mϕrup, S., Bϕdker, F., Van Wonterghem, J. and Madsen, M.B., Hyp. Int.51 (1989) 1071.

[Mϕ90] Mϕrup, S., Hyp. Int.60 (1990) 959.

[Mü80] Müller, E.W. MOSFUN, A New and Versatile Mössbauer Fitting Program distributed by the Mössbauer Effect Data Center, 1980.

[Na86] Nasu, S., Kurimoto, K., Nagatomo, S., Endo, S. and Fujita, F.E., Hyp. Int.29 (1986) 1583.

[Ni63] Nicol, M. and Jura, G. Science 141 (1963) 1035.

[Ok69] Ok, H.N., Phys.Rev. 181 (1969) 563.

[Pa90] Pavel, E., Baluta, Gb., Barb, D. and Lazar, D.P., Solid State Commun. 76 (1990) 531.

[Pe90] Perry, J., Nelson, S. and Hosomi, S., Material Res. Bulletin. (USA) 25 (1990) 749.

[Pi64] Pipkorn, D.N., Edge, C.K., Debrunner, P., Pasquali, de.G., Drickhamer, H.G. and Frauenfelder, H., Phys. Rev. 135 (1964) A1604.

[Po61] Pound, R.V., Benedek, G.B. and Drever, R., Phys. Rev. Lett. 7 (1960) 405.

[Pu89] Putyatin, A.A., Makarova, O.V. and Semenenko, K.N., Sverkhtverd. Mater. 11 (1989) 3.

[Ra83] Raudies, J.H., Appel, H., Then, G.M., Thies, W.G., Frietag, K., Sellschop, J.P.F. and Stemmet, M.E., Hyp. Int. 15/16 (1983) 487.

[Sa81] Sawicka, B.D., Sawicki, J.A. and Waard, H. de., Phys. Lett. 85A (1980) 153.

[Sa82] Saegusa, N and Morrish, A.H., Phy. Rev. B26 (1982) 308.

[Sa83] Sawicki, J.A., Sawicka, B.D. and Waard, de H., Hyp. Int. 15/16 (1983) 483.

[Sa90] Sawicki, J.A. and Sawicka, B.D., Phys. Rev. B 46 (1990) 38.

[S-H92] Sideras-Haddad, E., Connell, S.H., Sellschop, J.P.F., Bharuth-Ram, K., Stemmet, M.C., Naidoo, S. and Appel, H., Nucl. Instrum. Methods Phys. Res. B64 (1992) 237.

[Ta90] Taylor, R.D. and Pasternak, M.P., Hyp. Int. 53 (1990) 159.

[Ta91] Taylor, R.D. and Pasternak, M.P., J. Appl. Phys. 69 (1991) 6126.

[Ts84] Tsuzuki, A., Sago, S., Hirano, S. and Naka, S., J. Mat. Sc. 19 (1984) 2513.

[We79] Wedlake, R.J. : In The Properties of Diamond, ed., Field, J.E. (Academic Press, London, 1979).

[Ya90] Yarbrough, W. A. and Messier, R., Science 247 (1990) 688.